UC Berkeley

Title

The Translation Inhibitor Rocaglamide Targets a Bimolecular Cavity between eIF4A and Polypurine RNA

Permalink

Journal

ISSN

Authors

Iwasaki, Shintaro
Iwasaki, Wakana
Takahashi, Mari
et al.

Publication Date

DOI

Peer reviewed

The Translation Inhibitor Rocaglamide Targets a Biomolecular Cavity between eIF4A and Polypurine RNA

Shintaro Iwasaki[1,2,3,15,*], **Wakana Iwasaki**[4,5,14], **Mari Takahashi**[4,5,14], **Ayako Sakamoto**[4,5], **Chiduru Watanabe**[5,6], **Yuichi Shichino**[2], **Stephen N. Floor**[1,7,8], **Koichi Fujiwara**[9], **Mari Mito**[2], **Kosuke Dodo**[9,10,11], **Mikiko Sodeoka**[9,10,11], **Hiroaki Imataka**[12], **Teruki Honma**[5,6], **Kaori Fukuzawa**[13], **Takuhiro Ito**[4,5,*], and **Nicholas T. Ingolia**[1,*]

[1]Department of Molecular and Cell Biology, University of California, Berkeley, CA 94720 USA.

[2]RNA Systems Biochemistry Laboratory, RIKEN Cluster for Pioneering Research, Wako, Saitama, 351-0198 Japan

[3]Department of Computational Biology and Medical Sciences, Graduate School of Frontier Sciences, The University of Tokyo, 277-8561 Japan

[4]Laboratory for Translation Structural Biology, RIKEN Center for Biosystems Dynamics Research, Tsurumi-ku, Yokohama 230-0045, Japan

[5]Division of Structural and Synthetic Biology, RIKEN Center for Life Science Technologies

[6]Laboratory for Structure-Based Molecular Design, RIKEN Center for Biosystems Dynamics Research, Tsurumi-ku, Yokohama 230-0045, Japan

[7]Department of Cell and Tissue Biology, University of California, San Francisco, CA 94143 USA.

[8]Helen Diller Family Comprehensive Cancer Center, University of California, San Francisco, CA 94143 USA.

[9]Synthetic Organic Chemistry Laboratory, RIKEN Cluster for Pioneering Research, Wako, Saitama, 351-0198 Japan

[10]AMED-CREST, Japan Agency for Medical Research and Development

[11]RIKEN Center for Sustainable Resource Science, Wako, Saitama, 351-0198 Japan

[12]Graduate School of Engineering, University of Hyogo, Himeji, Hyogo 671-2201, Japan

[13]School of Pharmacy and Pharmaceutical Sciences, Hoshi University, Shinagawa, Tokyo 142-8501, Japan

[14]These authors contributed equally to this work

[15]Lead Contact

Summary

A class of translation inhibitors, exemplified by the natural product Rocaglamide A (RocA), isolated from *Aglaia* genus plants, exhibits antitumor activity by clamping eukaryotic translation initiation factor 4A (eIF4A) onto polypurine sequences in mRNAs. This unusual inhibitory mechanism raises the question of how the drug imposes sequence selectivity onto a general translation factor. Here, we determined the crystal structure of the human eIF4A1•ATP analog•RocA•polypurine RNA complex. RocA targets the "bi-molecular cavity" formed characteristically by eIF4A1 and a sharply bent pair of consecutive purines in the RNA. Natural amino acid substitutions found in *Aglaia* eIF4As changed the cavity shape, leading to RocA resistance. This study provides an example of an RNA sequence-selective interfacial inhibitor fitting into the space shaped cooperatively by protein and RNA with specific sequences.

Graphical Abstract
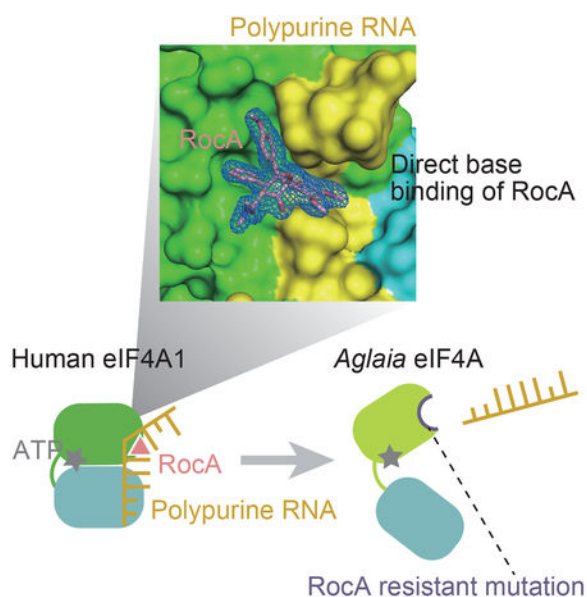
Introduction

Small molecule compounds that directly target RNAs have recently attracted great interest and promise a new avenue for drug development, providing an alternative path to targeting undruggable proteins or macromolecules (Mullard, 2017). Despite a variety of efforts, however, only few small molecules have been found that act in this way.

RocA and related rocaglates typify a distinctive group of mRNA-targeting compounds that block the translation from a subset of transcripts (Wolfe et al., 2014; Rubio et al., 2014;

Iwasaki et al., 2016). RocA was originally identified from the Meliaceae family plant *Aglaia* and is known as a natural insecticide (Li-Weber, 2015). Uniquely, RocA traps eukaryotic initiation factor (eIF) 4A — the prototypical DEAD-box protein (Rogers et al., 2002) — on polypurine RNA selectively, bypassing the ATP-requirement for RNA binding (Iwasaki et al., 2016). These stable eIF4A•RocA complexes block scanning ribosomes and consequently repress translation from the targeted mRNAs. In addition, the dissociation of eIF4A from the eIF4F complex — a heterotrimer of eIF4A, eIF4E, and eIF4G (Hinnebusch et al., 2016) — was also suggested as a mechanism of RocA-mediated translation repression (Cencic et al., 2009). Independent chemical screens identified RocA as a top hit for killing cancer cells displaying aneuploidy (Santagata et al., 2013) as well as those driven by oncogenic MYC activation (Manier et al., 2017). Rocaglates have been under active development as lead anti-cancer drugs tested in a number of pre-clinical mouse models (Bordeleau et al., 2008; Cencic et al., 2009; Santagata et al., 2013; Wolfe et al., 2014; Manier et al., 2017).

As exemplified by RocA, compounds that inhibit protein synthesis and its regulation are appealing therapeutic agents in cancer, as dysregulated translation can lead to tumorigenesis (Ruggero, 2013). In general, translation initiation is the rate-limiting step in protein synthesis (Morisaki et al., 2016; Wang et al., 2016; Wu et al., 2016; Yan et al., 2016), and translation initiation factors are subject to extensive physiological regulation (Sonenberg and Hinnebusch, 2009). Many eIFs assemble with the small (40S) ribosomal subunit into a 43S pre-initiation complex, which scans for the first AUG codon on an mRNA and then joins with a large (60S) subunit to form an active 80S ribosome on this start codon. eIF4A (Rogers et al., 2002) is recruited to the 5′ cap of an mRNA prior to 40S binding as a part of eIF4F complex, and is thought to play a key role in facilitating 43S complex scanning (Sonenberg and Hinnebusch, 2009; Hinnebusch et al., 2016). The eIF4F complex is a target of diverse natural and artificial compounds, including rocaglates, that disrupt the molecular processes underlying translation initiation and thereby show potential as anti-cancer therapies (Malina et al., 2012). Since many DEAD-box proteins act as RNA helicases, it is often proposed that eIF4A removes RNA structure in the 5′ UTR that would otherwise impair the progress of the pre-initiation complex (Svitkin et al., 2001). However, recent genome-wide studies using ribosome profiling (Ingolia et al., 2009; Ingolia et al., 2012; McGlincy and Ingolia, 2017) indicated that it has functions beyond the unwinding of RNAs (Sen et al., 2015; Iwasaki et al., 2016).

Understanding the structural mechanism of RocA's sequence selectivity and affinity promises to aid in developing derivatives for clinical use in cancer and, more broadly, provides a rational way for structure-based drug designs to target specific RNA sequences. Furthermore, although the biosynthesis of this translation inhibitor in *Aglaia* suggested that the plant must somehow avoid perturbing its own translation, the mechanism underlying this resistance has remained unclear. Here we solved the crystal structure of the quaternary complex consisting of RocA, human eIF4A1, the ATP analog AMPPNP, and polypurine RNA and showed that RocA targets the molecular interface formed between the eIF4A1 protein and polypurine bases at the sharply bent RNA bound on eIF4A1. By combining *de novo* assembly of the *Aglaia* transcriptome, ribosome profiling, and biochemical experiments, we also demonstrated that *Aglaia* has distinct RocA-resistance amino acid substitutions at the RocA binding site on its eIF4As. In elucidating the structural basis and

the resistance by this sequence selective translation inhibitor, we provided an example of an interfacial inhibitor exhibiting strong RNA sequence selectivity.

Results

Overall structure of the human eIF4A1•AMPPNP•RocA•(AG)$_5$ complex

To investigate the structural basis of the RNA selectivity provided by RocA (Figure S1A), we first set out to optimize the lengths of polypurine RNAs for crystallography, since excessively long RNAs will contain flexible regions that should be avoided. We prepared recombinant human eIF4A1, the most abundant and widely expressed eIF4A paralog, and measured its affinities to various AG repeat RNAs in a range of 6–20 nucleotides (nt) with AMPPNP as a nonhydrolyzable ATP analog along with RocA (Figure S1B–D). Although an apparent trade-off between RNA length and affinity was observed, we selected 10 nt (AG)$_5$ RNA for crystallography. RNAs of the same length have been crystallized in complexes with other DEAD-box proteins (Sengoku et al., 2006; Del Campo and Lambowitz, 2009).

Indeed, we successfully determined the crystal structure of the quaternary complex composed of eIF4A1•AMPPNP•RocA•(AG)$_5$ at 2.0-Å resolution (Figure 1A and Table 1). The N-terminal and C-terminal domains (NTD and CTD) of eIF4A1 were in a closed conformation around AMPPNP and formed an ATPase-active conformation (Sengoku et al., 2006). In the crystal structure, the eight RNA residues from G2 to A9 contacted eIF4A1 directly (Figure S2A). Strikingly, RocA was located between the eIF4A1 NTD and polypurine RNA, fitting into the cavity constructed by both macromolecules (Figure S2B). The RNA backbone bent sharply (Figure S2C), in a conformation that is characteristic of single-stranded RNAs bound to DEAD-box proteins in an ATP-bound state (Figure S2D and S2E) (Sengoku et al., 2006; Andersen et al., 2006; Del Campo and Lambowitz, 2009).

In spite of the presence of RocA, eIF4A1 and the polypurine RNA interacted in a very similar manner to that seen in other DEAD-box protein•RNA complexes, such as the Vasa•AMPPNP•polyU complex (Sengoku et al., 2006) (Figures S2D and S2E). Previously, only RNA-free eIF4A structures have been reported. As we provided the crystal structure of eIF4A bound to RNA, its resemblance to other DEAD-box proteins (Figures S2D and S2E) in the presence of RocA strongly suggested that the drug-free eIF4A•RNA interface is also quite similar. Moreover, the conformational similarity between the polypyrimidine RNAs on other DEAD-box proteins and the polypurine RNA in this structure (Figure S2F) highlighted the RNA-backbone contact as a general feature of DEAD-box protein•RNA complexes.

Generally, DEAD-box proteins melt RNA secondary structures by kinking the bound single-stranded RNAs, which is incompatible with helix formation (Linder and Jankowsky, 2011). RocA appears to exploit this central structural feature of their molecular mechanism: it targets the RNA position where normal base stacking interactions are disrupted on the protein.

In order to quantitatively dissect the interactions between RocA and RNA/eIF4A1, we performed the Pair Interaction Energy Decomposition Analysis (PIEDA) based on the *ab initio* fragment molecular orbital (FMO) calculations (Fedorov and Kitaura, 2009; Fedorov

et al., 2012; Tanaka et al., 2014), which provides the energy terms for interactions between RocA and the fragmented parts of the RNA and eIF4A1 (Figure 1B and 1C). The computation revealed strong π-π and CH/π interactions of RocA to Phe163, Gln195, G8, and A7, represented as dispersion energy terms (Figure 1B and 1C). Furthermore, two hydrogen bonds between RocA-Gln195 and RocA-G8 significantly contributed to the complex formation, indicated in electrostatic and charge transfer energy terms (Figure 1B and 1C).

RocA•RNA interaction: purine selectivity induced by RocA

The location of RocA in the complex explains the RNA sequence selectivity induced by this drug. RocA is inserted between the two base moieties of the sharply-bent consecutive purines A7 and G8. Out of the three phenyl rings in RocA (Figrue S1A, phenyl rings A, B, and C), two rings, A and B, stacked with the adenine base of A7 and guanine base of G8 nearly in parallel, respectively (Figure 2A). A very large dispersion energy term from A7 indicated a strong π-π interaction between A7 and ring A of RocA (Figure 1C). If A7 is replaced by a pyrimidine (U or C), it is hard for phenyl ring A to stack tightly with the smaller pyrimidine base (Figure 2B and 2C). Moreover, as indicated by the PIEDA analysis, the hydrogen bond between 8b-OH of RocA and N7 of G8 was a main driver of purine selection (Figure 1B and 1C). If G8 is substituted for pyrimidine, then this purine-selective hydrogen bond is not formed (Figure 2B and 2C). Because of the loss of the hydrogen bond and the weakened contacts by pyrimidines, only purine bases can form the bimolecular cavity to accommodate RocA. RocA-derivative compounds with modifications on the phenyl rings A and B and/or the 8b-OH group may change the shape and character of the bimolecular cavity, and thereby provide an alternative base selectivity.

RocA•eIF4A interaction explains reported resistance mutations

The third phenyl ring C of RocA anchors the drug to eIF4A. This ring C was sandwiched between the side-chains of Phe163 and Gln195 and surrounded by Gly160, Pro159, Ile199, and Asp198 (Figure 2A). As indicated by the PIEDA analysis (Figure 1B and 1C), the CO group of the 2-*N*,*N*-dimethyl-carboxamide in RocA formed the sole hydrogen bond to eIF4A1 via the side-chain NH_2 group of Gln195 (Figure 2A).

Remarkably, the structure can explain the RocA-resistant mutations found in yeast eIF4A. Sadlish *et al.* screened eIF4A mutants, which confer viability to yeast in the presence of the lethal concentration of rocaglates (Sadlish et al., 2013). The isolated mutations overlapped with the exact residues accommodating RocA in the structure: Pro159, Phe163, Phe192, Gln195, and Ile199.

Distinctive amino acid substitutions in Aglaia eIF4A

eIF4A is conserved in all eukaryotes. Therefore, we hypothesized that *Aglaia* must have evolved amino acid substitutions in eIF4A to avoid self-toxicity. However, the RocA-binding site on eIF4A revealed by our structure is highly conserved (Figure 3A), suggesting it is important for normal eIF4A function in translation. It was thus unclear how *Aglaia* avoids RocA toxicity while preserving eIF4A function. Since no genomic data on *Aglaia* were available, we sequenced rRNA-depleted mRNAs from the leaves of *Aglaia odorata* (Figure

S3A and S3B), and assembled the transcriptome *de novo*. The functional annotation of assembled transcripts identified ~50 DEAD-box protein genes (Figure S3C and Table S1), including three different copies of eIF4A.

Indeed, we found that *Aglaia* eIF4A is resistant to RocA. ATP-independent and polypurine-selective RNA clamping by eIF4A1 is a hallmark effect of RocA (Iwasaki et al., 2016). Recombinant protein produced from an *Aglaia* eIF4A gene (Figure S4A) did not show enhanced clamping on polypurine RNA by RocA regardless of ATP analogs (Figure 3C).

We further found that all three *Aglaia* eIF4As share the same substitutions — Phe163 to Leu and Ile199 to Met (amino acid position in human eIF4A1) — whereas the corresponding residues are well conserved among other eukaryotes, ranging from humans to plants (Figure 3A and 3B). We also assembled the eIF4A sequences *de novo* from another Meliaceae family member, *Azadirachita indica* (known as neem) (Figure S3D), using its published transcriptome data (Krishnan et al., 2012). We identified three *Azadirachita* eIF4A homologs and found that none of them possess the amino acid substitutions that occurred in *Aglaia* (Figure 3B), suggesting that the substitutions are quite specific to *Aglaia*.

The two residues mutated in *Aglaia* eIF4As, Phe163 and Ile199, were located immediately adjacent to RocA in the crystal structure (Figure 3D). If Phe163 is replaced by Leu, the methyl group of δ1 or δ2 in any possible rotamer is likely to reduce the space available in this RocA-binding pocket. In other words, *Aglaia* could avoid RocA-mediated translation inhibition by changing the shape of the eIF4A side of the bimolecular pocket.

The exact same amino acid changes of Phe163Leu and Ile199Met were reported to confer rocaglate-resistance in yeast and mouse (Sadlish et al., 2013; Chu et al., 2016), although polypurine RNA-specific effects of RocA on those mutants were not studied. Here, we showed that these artificial substitutions occur naturally in the *Aglaia* plant.

The eIF4A1 Phe163Leu-Ile199Met renders human cells resistant to RocA

The correspondence between amino acid substitutions in *Aglaia* eIF4As and the structural analysis of RocA binding led us to test the impact of mutating Phe163 to Leu and Ile199 to Met on human eIF4A1, which is sensitive to RocA. We purified the wild-type, Phe163Leu, Ile199Met, and double mutant recombinant proteins of human eIF4A1 (Figure S4A) and tested a variety of their biochemical properties: ATP binding, ATP hydrolysis, RNA binding, double-stranded RNA unwinding, and formation of the eIF4F complex (Figure S4B–G). Although reduced unwinding activity was observed in Phe163Leu and double Phe163Leu-Ile199Met mutant, all the assays showed that neither single nor double mutations disrupt the basic features of eIF4A1.

To further investigate the *in vivo* function of the mutated eIF4A1, we generated an HEK293 cell line, in which endogenous eIF4A1 is replaced with exogenous mutated eIF4A1. We first integrated exogenous eIF4A1 bearing an N-terminal streptavidin-binding peptide (SBP) tag and the double Phe163Leu-Ile199Met mutations through the Flp-In system (O'Gorman et al., 1991; Buchholz et al., 1996) into an HEK293 cell line with a single Flp recombination target (FRT) site (hereafter denoted as "naïve" HEK293) in the genome. The recombined

cell line [denoted as "SBP-eIF4A1 (Phe163Leu-Ile199Met)" HEK293] was subjected to CRISPR/Cas9–mediated knock-out of endogenous eIF4A1, with a single guide RNA spanning an exon-intron junction (Figure S5A and S5B). Although HEK293 cells are karyotypically abnormal and contain four copies of chromosome 17, where the eIF4A1 gene is located, we obtained a clonal cell line in which all four alleles contained indels (insertions and deletions) that introduced premature termination codons [denoted as "SBP-eIF4A1 (Phe163Leu-Ile199Met) *eIF4A1^SINE*" HEK293] (Figure S5A and S5B).

We found that eIF4A1 with the double mutations was able to complement wild-type eIF4A1 (Figure 4A). The isolated cell line showed neither defects in cell growth (Figure S5C) nor reductions in the global rate of protein synthesis measured by metabolic labeling with O-propargyl-puromycin (OP-puro), a CLICK reaction-compatible puromycin derivative (Figure S5D).

In contrast to its rescue of normal eIF4A1 function, double mutant eIF4A1 impacted the translational repression induced by RocA. We noted first that the complemented cells with double mutant eIF4A1 were desensitized to RocA-induced cell death (Figure 4B). Similar results have been reported in yeast and mouse cells bearing only a single Phe163Leu mutation in eIF4A (Sadlish et al., 2013; Chu et al., 2016). Ribosome profiling (Ingolia et al., 2009; Ingolia et al., 2012; McGlincy and Ingolia, 2017), a genome-wide translatome analysis by deep sequencing of ribosome footprints, showed that the RocA-induced global translation repression was weaker in mutant cells than in their naïve counterparts (Figure 4C). Metabolic peptide labeling by OP-puro validated this observation (Figure S5E).

Translational inhibition by RocA is not uniform across the transcriptome, but biased (Liu et al., 2012; Wolfe et al., 2014) toward a subset of mRNAs possessing polypurine motifs in their 5′ UTRs (Iwasaki et al., 2016). The double mutant eIF4A reduced this biased translation inhibition; ribosome profiling revealed that the repression of RocA-susceptible mRNAs is uniformly weaker in double mutant cells (Figure 4D). We further tested the loss of selective translation repression using a synthetic reporter with polypurine motifs in its 5′ UTR (Iwasaki et al., 2016). Strikingly, we observed that double mutant cells reduced the RocA sensitivity of the polypurine reporter but did not affect the negative control reporter with a CAA-repeat 5′ UTR (Figure 4E).

Phe163Leu-Ile199Met mutations abolish RocA-induced polypurine RNA clamping and translational repression

ATP-independent and polypurine RNA-selective clamping of eIF4A1•RocA complexes on 5′ UTRs sterically hinders 43S ribosome scanning (Iwasaki et al., 2016). Given the RocA resistance provided by the double mutation in human cells, we reasoned that double mutant eIF4A1 must lose the high-affinity, persistent RNA binding normally induced by RocA treatment. Indeed, we found that ATP-independent clamping of recombinant eIF4A1 onto polypurine RNA was lost in the double mutant eIF4A1 *in vitro* (Figure 5A). The single Phe163Leu mutation also perturbed the RocA-mediated clamp onto polypurine RNA, whereas we observed only a modest effect from the Ile199Met mutation (Figure 5A).

Consistent with its inability to clamp onto polypurine RNA, double mutant eIFA1 is deficient for RocA-mediated translation repression. To investigate translation repression by RocA *in vitro*, we first pre-incubated recombinant eIF4A1 and RocA with an mRNA bearing polypurine motifs. This pre-incubation allowed eIF4A1•RocA complexes to form on the polypurine tracts, where they could be monitored by toeprinting assay (Figure 5B) (Iwasaki et al., 2016). After removal of free RocA by gel filtration, the mRNA with eIF4A1•RocA complexes was translated *in vitro* by rabbit reticulocyte lysates. As previously reported (Iwasaki et al., 2016), the preformation of the complex between WT eIF4A1 and RocA (Figure 5B, top) recapitulated RocA-mediated translation repression (Figure 5C). On the other hand, the double mutant neither formed stable complex on the mRNA (Figure 5B, bottom) nor repressed translation from the mRNA (Figure 5C).

Furthermore, we directly tested the capacity of double mutant eIF4A1 for RocA-mediated translation repression in a reconstituted eukaryotic translation system. Crude lysate systems for *in vitro* translation do not permit the easy substitution of essential translation factors. This led us to use a pure reconstitution system for cap-dependent translation with human factors, which we recently established (Machida et al., 2018) (T. Yokoyama, K. Machida, W. Iwasaki, T. Shigeta, M. Nishimoto, M. Takahashi, A. Sakamoto, M. Yonemochi, Y. Harada, H. Shigematsu, M. Shirouzu, H. Tadakuma, H. Imataka, and T. Ito, personal communication). Harnessing the requirement for eIF4F in this system, we replaced WT eIF4A1 with our *Agiala* mutant, and then tested the sensitivity of translation from mRNAs with polypurines. Whereas dose-dependent translation repression by RocA was recapitulated with WT eIF4A1 protein, double mutant eIF4A1 conferred RocA resistance to the pure system (Figure 5D).

RocA targets a RNA sequence-specific interface on eIF4A1

The straightforward interpretation of these data was that the Phe163Leu and Ile199Met mutations block RocA binding to eIF4A1. In order to directly examine the importance of *Aglaia*-specific amino acid substitutions in the eIF4A1•RocA interaction, we performed nuclear magnetic resonance spectroscopy (NMR) of ^{15}N-labeled eIF4A1 NTD, since RocA could artificially clamp the isolated NTD onto polypurine RNA (Iwasaki et al., 2016). We observed chemical shift perturbations of some residues in the wild-type NTD upon RocA addition (Figure 6A, 6B and S6). In contrast, the double mutant of the NTD exhibited little chemical shift perturbation upon RocA addition (Figure 6A, 6B, and S6), indicating the loss of the RocA•eIF4A1 interaction. However, we noted that aspects of our NMR experiments — truncated eIF4A1, the requirement of high concentration (sub millimolar) of RocA, and the absence of RNA — were not physiological.

Our structure suggested that RocA preferentially targets the cavity in the complex formed with eIF4A1 and polypurine RNA, and not the protein in isolation (Figure 2). To biochemically test this model, we placed a biotin handle on RocA at the dimethylamide group (Figure S1A, S1E, and S1F), which did not contact either RNA or eIF4A1 in our structure (Figure 2A); this modification was previously reported to preserve RocA activity (Chambers et al., 2016). The recombinant eIF4A1 protein and the polypurine RNA were co-purified with the RocA-biotin on streptavidin beads, whereas either double mutant eIF4A1

or non-target RNA lacking polypurine motifs abolished the co-purification (Figure 6C). The striking correspondence between our structural observations (Figure 2A) and this pulldown assay (Figure 6C) indicated that the formation of the interface between Phe163 on eIF4A1 and polypurine RNA is a prerequisite for RocA targeting.

Discussion

RocA has been shown to act as an mRNA-selective translation inhibitor (Rubio et al., 2014; Wolfe et al., 2014; Rubio et al., 2014; Wolfe et al., 2014; Iwasaki et al., 2016). Now, we have presented clear molecular insights into the RNA sequence selectivity of RocA and the RocA resistance in *Aglaia* (Figure 6D). Whenever ATP-bound eIF4A binds to RNA and kinks it to induce unwinding, a bimolecular cavity is formed between the eIF4A NTD and the bent single-stranded RNA. When human eIF4A1 binds to consecutive purine residues, the resultant bimolecular cavity can accommodate RocA, as revealed in our crystal structure (Figure 6D, top). This eIF4A•RocA•polypurine complex is so stable that this complex is likely to persist even after ATP hydrolysis, as we observed in our earlier study (Iwasaki et al., 2016), leading to translation repression. If either one of two adjacent purines is replaced by a pyrimidine, the resultant cavity cannot accommodate RocA, because the contact between RNA and RocA is weakened (Figure 6D, middle). In *Aglaia*, the amino acid substitutions of Phe163Leu and Ile199Met (in human eIF4A1 numbering) change the shape of the cavity and RocA does not fit into the interface even in the presence of polypurine RNA (Figure 6D, bottom). Therefore, *Aglaia* avoids poisoning itself despite biosynthesizing a potent natural inhibitor of translation. Although we found two amino acid substitutions at Phe193Leu and Ile199Met in *Aglaia* eIF4As, the single mutation in Phe163, where RocA directly associates, provides substantial RocA resistance to sensitive human eIF4A1. Although Ile199 does not directly accommodate RocA in the structure, it is most likely that it supports the favorable rotameric orientation of Phe163 for the association with RocA. Indeed, we observed modest resistance in ATP-independent polypurine RNA clamping from the single Ile199Met mutation (Figure 5A).

Whereas Phe163Leu-Ile199Met mutations clearly rendered human eIF4A1 resistant to RocA *in vitro* (Figure 5), their *in vivo* effects were still modest (Figure 4). This difference was probably caused by the presence of a highly homologous eIF4A1 paralog, eIF4A2, which has been also reported as a target of rocaglates (Chambers et al., 2013; Chambers et al., 2016). Although its expression is relatively low compared to eIF4A1 in the HEK293 cells used in this study (Figure S5F), the potent dominant negative effect of RocA (Iwasaki et al., 2016) could be induced via the minor paralog of eIF4A.

RocA provides a distinctive example of an RNA sequence-specific interfacial inhibitor: this small compound functions as glue to trap eIF4A selectively onto certain RNA sequences. Targeting a molecular interface is a general strategy for natural compounds to block the normal function of a macromolecule. Indeed, inhibitors bound to a protein-nucleic acids interface have been found in diverse macromolecular complexes (Pommier et al., 2015). Uniquely, RocA also binds in this manner, but only when it can be accommodated by the cavity shaped by a specific RNA sequence. Since a typical low-to-medium molecular weight drug inhibits the interaction between the target molecule and some other partner (e.g., an

enzyme-substrate interaction, a receptor-ligand interaction, or a protein-protein interaction), most drug screening systems are designed to detect the loss of an interaction. Our elucidation of the sophisticated RocA mechanism will encourage the development of novel strategies to screen drugs targeting macromolecular complexes, such as single stranded-RNA binding proteins, which generally possess cavities between proteins and RNAs.

STAR METHODS

KEY RESOURCES TABLE

REAGENT or RESOURCE	SOURCE	IDENTIFIER
Antibodies		
Rabbit polyclonal anti-eIF4A1	Cell Signaling Technology	Cat#2490S; RRID: AB 823487
Rabbit polyclonal anti-eIF4A2	Abcam	Cat#ab31218; RRID: AB 732123
Mouse monoclonal anti-p-actin	LI-COR Biosciences	Cat#926–42212
Mouse monoclonal anti-SBP-tag (SB19-C4)	Santa Cruz Biotechnology	Cat#sc-101595; RRID: AB_1128239
IRDye 800CW goat polyclonal anti-rabbit IgG	LI-COR Biosciences	Cat#926–32211; RRID: AB 621843
IRDye 680RD Goat anti-Mouse IgG	LI-COR Biosciences	Cat#925–68070; AB_2651128
Bacterial and Virus Strains		
E. coli: T7 Express cells	New England Biolabs	Cat#C2566H
E. coli: BL21 (DE3)	Nippongene	Cat#318–06531
E. coli: BL21 Star (DE3)	ThermoFisher Scientific	Cat#C601003
Chemicals, Peptides, and Recombinant Proteins		
Rocaglamide A (RocA)	Sigma-Aldrich	Cat#SML0656–100UG
RocA-biotin	This paper	N/A
Recombinant protein: eIF4A1 (19–406)	This paper	N/A
Recombinant protein: eIF4A1 (WT)	This paper	N/A
Recombinant protein: eIF4A1 (Phe163Leu)	This paper	N/A
Recombinant protein: eIF4A1 (Ile199Met)	This paper	N/A
Recombinant protein: eIF4A1 (Phe163Leu-Ile199Met)	This paper	N/A
Recombinant protein: A.orodata eIF4A-1 iso2	This paper	N/A
Recombinant protein: eIF4A1 NTD (WT)	This paper	N/A
Recombinant protein: eIF4A1 NTD (Phe163Leu-Ile199Met)	This paper	N/A
HisTrap HP column 5 ml	GE Healthcare	Cat#17524802
HiTrap Heparin HP column 5 ml	GE Healthcare	Cat#17040703
HiTrap Heparin HP column 1 ml	GE Healthcare	Cat#17040601
Superdex 200 Increase 10/300 GL column	GE Healthcare	Cat#28990944
AMPPNP	Roche	Cat#10102547001
Ni-NTA Superflow	Qiagen	Cat#30410
Critical Commercial Assays		
RNeasy Plant Mini kit	Qiagen	Cat#74903
RiboMinus Plant kit for RNA-Seq	ThermoFisher Scientific	Cat#A1083808

REAGENT or RESOURCE	SOURCE	IDENTIFIER
TruSeq Standard Total RNA Library Prep Kit	Illumina	Cat#RS-122–2301
RealTime-Glo MT Cell Viability Assay	Promega	Cat#G9711
Deposited Data		
Ribosome profiling, raw and analyzed data	This paper	GEO: GSE102720
RNA-Seq, raw data	This paper	SRA: SRR5947159
Human eIF4A^AMPPNP^RocA^(AG)$_5$ complex structure	This paper	PDB: 5ZC9
Mendeley Database	This paper	https://data.mendeley.com/datasets/z9c8mn82k5/draft?a=693ee
Experimental Models: Cell Lines		
T-REx293 (HEK)	ThermoFisher Scientific	Cat#R71007
T-REx293 SBP-eIF4A1 (WT)	Iwasaki *et al.* 2016	N/A
T-REx293 SBP-eIF4A1 (Phe163Leu)	This paper	N/A
T-REx293 SBP-eIF4A1 (Ile199Met)	This paper	N/A
T-REx293 SBP-eIF4A1 (Phe163Leu-Ile199Met)	This paper	N/A
T-REx293 SBP-eIF4A1 (Phe163Leu-Ile199Met) eIF4A 1^{SINI}	This paper	N/A
Oligonucleotides		
FAM labeled RNA (AG)k,: FAM-AGAGAGAGAG AGAGAGAGAG	This paper	N/A
FAM labeled RNA (AG)s: FAM-AGAGAGAGAG	This paper	N/A
FAM labeled RNA (AG)4: FAM-AGAGAGAG	This paper	N/A
FAM labeled RNA (AG)s: FAM-AGAGAG	This paper	N/A
Polypurine RNA sequence: AGAGAGAGAG	This paper	N/A
Unwinding assay RNA: GCGUCUUUACGGUGCU UAAAACAAAACAAAACAAA ACAAAA	This paper	N/A
Unwinding assay RNA: AGCACCGUAAAGACGC	This paper	N/A
Recombinant DNA		
pRARE2	Novagen-Merck	N/A
pET47-eIF4A1 –19–406	This paper	N/A
pcDNA5/FRT/TO-SBP-eIF4A1 WT	Iwasaki *et al.* 2016	N/A
pcDNA5/FRT/TO-SBP-eIF4A1 Phe163Leu	This paper	N/A
pcDNA5/FRT/TO-SBP-eIF4A1 Ile199Met	This paper	N/A
pcDNA5/FRT/TO-SBP-eIF4A1 Phe163Leu-Ile199Met	This paper	N/A
pColdI-eIF4A1 WT	This paper	N/A
pColdI-eIF4A1 Phe163Leu	This paper	N/A
pColdI-eIF4A1 Ile199Met	This paper	N/A
pColdI-eIF4A1 Phe163Leu-Ile199Met	This paper	N/A
pColdI-Ao-eIF4A-1 iso2	This paper	N/A
pHISMBP-eIF4A1-NTD (WT)	Iwasaki *et al.* 2016	N/A
pHISMBP-eIF4A1-NTD (Phe163Leu-Ile199Met)	This paper	N/A
Software and Algorithms		

REAGENT or RESOURCE	SOURCE	IDENTIFIER
Igor Pro Version: 8.01	WaveMetrics	https://www.wavemetrics.com/products/igorpro
Coot	Emsley *et al.*, 2004	https://www2.mrc-lmb.cam.ac.uk/personal/pemsley/coot/
Phenix	Adams *et al.*, 2010	https://www.phenix-online.org/
PyMOL	Schrodinger	https://pymol.org/
NMRPipe	Delaglio *et al.*, 1995	https://www.ibbr.umd.edu/nmrpipe/install.html
Sparky	T.D. Goddard and D.G. Kneller, University of California, San Francisco, CA	https://www.cgl.ucsf.edu/home/sparky/
Trinity	Grabherr *et al.*, 2011	https://github.com/trinityrnaseq/trinityrnaseq/wiki
Trinotate	Haas *et al.*, 2013	https://github.com/Trinotate/Trinotate.github.io/wiki
ESPript 3.0	Robert and Gouet, 2014	http://espript.ibcp.fr
AAcon	University of Dundee	http://www.compbio.dundee.ac.uk/aacon/
Clustal Omega	EMBL-EBI	https://www.ebi.ac.uk/Tools/msa/clustalo/

CONTACT FOR REAGENT AND RESOURCE SHARING

Further information and requests for resources and reagents should be directed to the Lead Contact, Shintaro Iwasaki (shintaro.iwasaki@riken.jp).

EXPERIMENTAL MODEL AND SUBJECT DETAILS

Cell lines and culture condition—T-Rex-293 (HEK) cells (ThermoFisher Scientific) were cultured in DMEM (1×) + GlutaMAX-I supplemented with 10% FBS.

Integrations of SBP-eIF4A1 (Phe163Leu), SBP-eIF4A1 (Ile199Met), and SBP-eIF4A1 (Phe163Leu-Ile199Met) into T-Rex-293 were performed with the transfection of pcDNA5/FRT/TO-SBP-eIF4A1 (Phe163Leu-Ile199Met) and pOG44 (Thermo Fisher Scientific) and selected with Blasticidin S and Hygromycin B, according to manufacturer's instruction.

The guide RNA for CRISPR/Cas9 genome editing was *in vitro* transcribed from the template PCR fragment (5′-TAATACGACTCACTATAGGCCTTTCTTACCGGGAATCCGTTTAAGAGCTATGCTGGAAACAGCATAGCAAGTTTAAATAAGGCTAGTCCGTTATCAACTTGAAAAAGTGGCACCGAGTCGGTGCTTTTTTT-3′) using T7-Scribe Standard RNA IVT kit (Cellscript), and purified by Agencourt RNAclean XP beads (Beckman Coulter). Twelve μM guide RNA and 10 μM recombinant Cas9-NLS protein (Macro lab, UC Berkeley) were incubated in 10 μl of 20 mM HEPES-KOH pH 7.5, 150 mM KCl, 10% glycerol, and 1 mM DTT at 25°C for 20 min. The RNP was nucleofected (Lin et al., 2014) into T-Rex-293 SBP-eIF4A1 (Phe163Leu-Ile199Met) integrant cultured with 1 μg/ml tetracycline, by Nucleofector 4d (Lonza) with program DS150 using SF media (Lonza), according to manufacturer's instruction. After five days post the nucleofection, cells were seeded at 0.3 cells/well in 96-well plates to isolate clonal population. Cells were screened by PCR with primers (5′-CTAACGTCATGCCGAGTTGC-3′ and 5′-TGGGCCACACATAGTGGC-3′,

spanning targeted genome region) to check the insertion and deletion by PCR and then further screened by western blot of eIF4A1. The PCR products from "SBP-eIF4A1 (Phe163Leu-Ile199Met) *eIF4A1*^{SINF}" HEK293 were cloned into TOPO Zero Blunt vector (ThermoFisher) and analyzed.

METHOD DETAILS

General materials—RocA was purchased from Sigma-Aldrich and dissolved in DMSO. RNA oligonucleotides labeled with FAM at 5′-end, were purchased from IDT and Hokkaido System Science.

Sample preparation for crystallization—*E. coli* T7 Express cells (New England Biolabs) were doubly transformed with pRARE2 (Novagen-Merck) and pET47-eIF4A1–19-406, which encodes the eIF4A1 fragment from Pro19 to C-terminal Ile406 with the N-terminal His-Tag and the HRV 3C cleavage site attached. The transformed cells were grown in lysogeny broth medium at 37°C to OD_{600} ~0.5. After the addition of 0.5 mM IPTG, the cells were grown at 20°C for 18 hr. The collected cells were lysed by sonication in 20 mM HEPES-KOH pH 7.5, 300 mM KCl, 20 mM imidazole, 5 mM β-mercaptoethanol, 0.1 mM EDTA, 10% (v/v) glycerol, and 1× Complete EDTA-free protein inhibitor (Roche). The lysate was fractionated on a HisTrap HP 5 ml column (GE Healthcare), followed by the tag cleavage with HRV 3C protease for overnight. The tag-cleaved protein was further fractionated by the HiTrap Heparin HP 5 ml and Superdex 200 Increase 10/300 GL columns (GE Healthcare). The purified protein was finally dissolved into 20 mM HEPES-KOH pH 7.5, 100 mM KCl, 5 mM $MgCl_2$, 1 mM DTT, 0.1 mM EDTA, and 10% (v/v) glycerol, and concentrated to 9.3 mg/ml using Amicon Ultra filter (Millipore-Merck).

The HPLC-grade RNA was commercially purchased (Fasmac, Japan). 9.3 mg/ml eIF4A1 was mixed with dried polypurine RNA (AGAGAGAGAG), as a molar ratio was 1:3. AMPPNP (Roche) and RocA were supplemented as their final concentration were 1 mM and 320 μM, respectively. The sample solution was mixed with an equal volume of the reservoir solution, consisting of 80 mM HEPES (pH 7.5), 1120 mM tri-sodium citrate, 100 mM ammonium sulfate, 20 mM Bis-Tris (pH 6.0), 0.2% (w/v) polyethylene glycol 3,350, and 40 mM lithium chloride. A crystallization drop was formed on an MRC-2 crystallization plate (Swissci) containing a 70-uL reservoir solution in the well, and incubated at 293 K. Crystals appeared within a few days, and they were flash-cooled with liquid nitrogen in a cryoprotectant reagent containing 30% (w/v) Tacsimate (pH 7.0) (Hampton Research).

RNA-Seq—*Aglaia odorata* leaves were flash-frozen with RLT buffer from RNeasy Plant Mini kit (Qiagen) by liquid nitrogen, and homogenized by cryogenic grinding with mixer mill (Retch) at 30 Hz for 3 min for 5 times. RNA was extracted using the RNeasy Plant Mini kit according to manufacturer's instruction. The electropherogram of purified RNA was obtained by TapeStation2200 (Agilent). Followed by rRNA depletion with RiboMinus Plant kit for RNA-Seq (ThermoFisher Scientific), the library was prepared by TruSeq Standard Total RNA Library Prep Kit (Illumina) and sequenced on HiSeq2500 (Illumina) sequencer.

DNA constructs

pcDNA5/FRT/TO-SBP-eIF4A1 WT, Phe163Leu, Ile199Met, and double Phe163Leu-Ile199Met: pcDNA5/FRT/TO-SBP-eIF4A1 was obtained by earlier study (Iwasaki et al., 2016). Phe163Leu and Ile199Met substitutions were introduced by site-directed mutagenesis.

pColdI-eIF4A1 WT, Phe163Leu, Ile199Met, and double Phe163Leu-Ile199Met: DNA fragments coding wild-type *EIF4AI* and its mutants were inserted into pColdI (Takara bio) via NdeI and HindIII sites.

pColdI-Ao-eIF4A-1 iso2: DNA fragments coding wild-type *Aglaia odorata eIF4A-1 iso2* was amplified from cDNA of *Aglaia odorata* leaves and its mutants were inserted into pColdI (Takara bio) via NdeI and HindIII sites.

pHISMBP-eIF4A1-NTD (WT) and eIF4A1-NTD (Phe163Leu-Ile199Met): Phe163Leu-Ile199Met was introduced into pHISMBP-eIF4A1-NTD (Iwasaki et al., 2016) by site-directed mutagenesis.

Cell proliferation/viability assay—HEK293 cells were seeded into white 96-well plate and incubated with RealTime-Glo MT Cell Viability Assay (Promega) at each time points of the measurements. The luminescence was detected by GloMax-96 (promega). For cell viability assay, cells were treated with RocA (0–10 nM) for 72 hr prior to the assay. Data were fitted by Igor Pro 8 (WaveMetrics).

Ribosome profiling—Control solvent DMSO (final concentration 0.1%) or 0.3 μM RocA was added to media 30 min prior to cell lysis. Lysates containing 10 μg RNA were treated with 20 units of RNase I (Epicentre) for 45 min at 25°C. The ribosomes were collected by sucrose cushion. The extracted RNAs ranging from 26 to 34 nt were selected from 15% UREA PAGE gel. Following dephosphorylation, 3′ linker-ligation, rRNA depeletion by RiboZero Gold (Illumine), reverse transcription, circularization, and PCR, the DNA libraries were prepared amplification (Ishikawa et al., 2017; McGlincy and Ingolia, 2017). The libraries were sequenced by HiSeq4000 (Illumina).

Purification of recombinant eIF4A1 proteins—*E. coli* BL21 (DE3) cells transformed with pColdI-eIF4A1 (WT), eIF4A1 (Phe163Leu), eIF4A1 (Ile199Met), or eIF4A1 (Phe163Leu-Ile199Met), or Ao-eIF4A-1 iso2 were cultivated to OD_{600} 0.5 at 37°C in 1 L culture with 100 μg/ml carbenicillin and then grown at 15°C overnight with 1 mM IPTG. The cell pellet was collected by centrifugation at 3,000 g for 20 min at 4°C, resuspended in His buffer (20 mM HEPES-NaOH pH 7.5, 500 mM NaCl, 10 mM imidazole, 10 mM β-mercaptoethanol, and 0.5% NP-40), sonicated, and clarified by centrifugation at 10,000 g for 20 min at 4°C. The supernatant was incubated with 1.5 ml bed volume of Ni-NTA Superflow (Qiagen) for 1 hr. The beads were transferred into Glass Econo-Column (Bio-Rad), washed by the flowing 20 ml of high salt wash buffer (20 mM HEPES-NaOH pH 7.5, 1 M NaCl, 20 mM imidazole, and 10 mM β-mercaptoethanol) twice and then 20 ml low salt wash buffer (20 mM HEPES-NaOH pH 7.5, 10 mM NaCl, 20 mM imidazole, and 10 mM β-

mercaptoethanol) once. The His-tagged protein was eluted with 7.5 ml of elution buffer (20 mM HEPES-NaOH pH 7.5, 10 mM NaCl, 250 mM imidazole, 10 mM β-mercaptoethanol, and 10% glycerol). Using AKTA purifier (GE Healthcare) or NGC Chromatography System (Bio-rad), the protein was loaded onto HiTrap Heparin HP column 1 ml (GE Healthcare) and eluted with linear gradient from buffer A (20 mM HEPES-NaOH pH 7.5, 10 mM NaCl, 0.5 mM TCEP, and 10% glycerol) to buffer B (buffer A with 1 M NaCl). The peaked fractions were collected, buffer-exchanged to 20 mM HEPES-NaOH pH 7.5, 150 mM NaCl, 10% glycerol, and 1 mM DTT by NAP-5 and PD-10 (GE Healthcare), concentrated with Amicon Ultra 10kDa (Millipore), shock-frozen in liquid nitrogen, and stored at −80°C. All purification steps were performed at 4°C.

ATP crosslinking assay—Ten μM of recombinant eIF4A1 proteins and 0.1 μM of γ ^{32}P-ATP (Perkinelmer) were incubated for 15 min at 37°C and then UV-exposed for 1500 mJ/cm^2 at 254 nm (Iwasaki et al., 2016). The complexes were separated in SDS-PAGE and the images were obtained by Amersham Typhoon IP (GE Healthcare).

Fluorescence polarization assay—The recombinant eIF4A1 proteins (0–50 μM) and 10 nM 5′ FAM-labeled RNAs are incubated with 0.1% DMSO or 50 μM RocA for 30 min at room temperature (Iwasaki et al., 2016). For ATP analogs, 1 mM AMP-PNP or 1 mM ADP with 1 mM Na$_2$HPO$_4$ were used. The fluorescent polarizations were measured by Infinite F-200 PRO (TECAN).

Unwinding assay—RNA duplex was prepared by annealing of 5′-GCGUCUUUACGGUGCUUAAAACAAAACAAAACAAAACAAAA-3′ and 5′-AGCACCGUAAAGACGC-3′, and short RNA strand was radiolabeled by γ ^{32}P-ATP (Perkinelmer) and T4 polynucleotide kinase (New England Biolabs) (Jankowsky and Putnam, 2010; Floor et al., 2016). In 30 l reaction scale, 10 M recombinant eIF4A1 and 20 nM of the radio-labeled RNA duplex was incubated in 40 mM Tris-HCl pH 7.5, 2 mM HEPES-NaOH pH 7.5, 15 mM NaCl, 2 mM ATP, 2.5 mM MgCl$_2$, 0.01% IGEPAL CA-630, 1% glycerol, 2 mM DTT, and 2 μM complementary DNA (5′-AGCACCGTAAAGACGC-3′) at 37°C. The reaction was quenched by an addition of equal amount of 2× Gel Loading Dye, Purple (New England Biolabs) and run on native TBE polyacrylamide gel, 20%. The images were obtained by Amersham Typhoon IP (GE Healthcare).

ATPase assay—In 20 μl reaction scale, 10 μM recombinant eIF4A1 and 0.25 μM γ ^{32}P-ATP (Perkinelmer) are incubated in 20 mM HEPES-NaOH pH 7.5, 150 mM NaCl, 10% glycerol, 1 mM DTT, and 1 mM MgCl$_2$ at 37°C. The reaction was quenched by adding the equal volume of 200 mM Tris-HCl, pH 7.5, 25 mM EDTA pH 8.0, 300 mM NaCl, and 2% sodium dodecyl sulfate (SDS), spot on thin layer chromatography plate (Polygram CEL 300 PEI / UV254, Macherey-Nagel), and developed by 0.45 M NH$_4$SO$_4$. The images were obtained by Amersham Typhoon IP (GE Healthcare).

Reporter assay in cells—Reporter RNAs were prepared by *in vitro* transcription, capping, and poly(A)-tailing (Iwasaki et al., 2016). The RNAs were transfected to T-

Rex-293 (HEK) cells by TransIT-mRNA (Mirus) (Iwasaki et al., 2016). The luminescence was measured by Renilla-Glo Luciferase Assay System (Promega).

Toeprinting assay—Ten μM of recombinant eIF4A1 proteins, 50 nM reporter mRNAs, 2 mM ATP, and 2 mM $MgCl_2$ were incubated for 5 min at 30°C in the presence or absence of 10 μM RocA. Then, cDNAs were synthesized by 10 U/l ProtoScript II (New England Biolabs) with 250 nM 5′ 6-FAM labeled DNA oligo (5′–6-FAM-ATGCAGAAAAATCACGGC-3′). Purified cDNAs were run on 3730 DNA Analyzer (Life Technologies) (Iwasaki et al., 2016).

***In vitro* translation in RRL followed by the complex preformation—**Following the eIF4A1 complex formation as describe above, the free RocA was removed by G-25 column (GE Healthcare). Flow-through mRNP complex was added to nuclease-treated RRL system (Promega). The luminescence was measured by Renilla-Glo Luciferase Assay System (Promega) (Iwasaki et al., 2016).

Preparation of NMR samples—pHISMBP-eIF4A1-NTD (WT) or eIF4A1-NTD (Phe163Leu-Ile199Met) were transformed into BL21 Star (DE3) cells and grown in four liters of M9 minimal media made with ^1H, natural abundance carbon glucose and $^{15}NH_4Cl$ (Cambridge Isotope Laboratories) at 37°C to OD_{600} ~0.5. Precursors for ^{13}C-methyl labeled isoleucine, leucine, valine, methionine and alanine residues (Cambridge Isotope Laboratories) were then added directly to the half of the culture flasks, as described (Floor et al., 2012). After 30 min of growth, cultures were moved to 4°C for 30 min and then expression was induced by adding 1 mM IPTG to the culture media and transferring to 16°C for 18 hr. Cells were harvested by centrifugation and the labeled proteins was purified as for unlabeled proteins.

NMR spectroscopy—Proteins were concentrated to ~200 μM in gel filtration buffer (20 mM HEPES-NaOH, pH 7.5, 150 mM NaCl, and 0.5 mM TCEP), supplemented with 7% D_2O (Cambridge Isotope Laboratories), and transferred to thin-walled Shigemi tubes. Nitrogen heteronuclear single quantum coherence (HSQC) (Mori et al., 1995) and carbon heteronuclear multiple quantum coherence (HMQC) (Mueller, 1979) experiments were acquired on a Bruker 900 MHz spectrometer equipped with a cryogenic probe at the Central California 900 MHz NMR facility. Resonances have not been assigned. Instead, NMR spectra collected in different conditions were compared to identify peaks that change in one condition but not another. Data were processed using NMRPipe (Delaglio et al., 1995), and visualization was performed using Sparky (T.D. Goddard and D.G. Kneller, University of California, San Francisco, CA). RMS normalized chemical shifts were calculated according to $\sqrt{(\Delta N/5)^2 + (\Delta H)^2}$ (Floor et al., 2012).

SBP-pulldown assay—HEK293 cells [naïve and integrants with SBP-eIF4A1 (WT) (Iwasaki et al., 2016), SBP-eIF4A1 (Phe163Leu), SBP-eIF4A1 (Ile199Met), or SBP-eIF4A1 (Phe163Leu-Ile199Met)] were cultured with 1 μg/ml of tetracycline in 10 cm dish for 3 days, washed with ice-cold PBS once, and then lysed with 600 μl of lysis buffer (20 mM Tris-HCl pH 7.5, 150 mM NaCl, 5 mM $MgCl_2$, 1 mM DTT, and 1% Triton-X 100). The

lysate was incubated with 60 μl of Dynabeads M270 Streptavidin (Thermo Fisher Scientific) equilibrated with lysis buffer at 4°C for 1 hr, and then washed with lysis buffer 5 times. Proteins were eluted by 20 μl of lysis buffer containing 5 mM biotin at 4°C for 30 min.

m^{7}GTP-affinity purification—HEK293 cells [integrants with SBP-eIF4A1 (WT) (Iwasaki et al., 2016) or SBP-eIF4A1 (Phe163Leu-Ile199Met)] were cultured with 1 μg/ml of tetracycline in 15 cm dish for 3 days, washed with ice-cold PBS once, and then lysed with 1200 μl of hypotonic lysis buffer (10 mM HEPES-NaOH pH 7.5, 10 mM KCl, 1.5 mM MgCl$_2$, 1 mM DTT, and 1× Protease Inhibitor Cocktail for Use with Mammalian Cell and Tissue Extracts [Nacalai]). The lysate was pre-cleared with 150 μl of Pierce Control Agarose Resin (Thermo Fisher Scientific) equilibrated with hypotonic lysis buffer, at 4°C for 1 hr. The pre-cleared lysate was incubated with 40 μl of Pierce Control Agarose Resin or γ-aminophenyl-m^{7}GTP (C10-spacer)-Agarose (Jena Bioscience) equilibrated with hypotonic wash buffer [10 mM HEPES-NaOH pH 7.5, 10 mM KCl, 1.5 mM MgCl$_2$, 1 mM DTT, 0.02% Triton-X 100, and 50 μg/ml tRNA from baker's yeast (Sigma-Aldrich)], at 4°C for 1 hr, and then washed with hypotonic wash buffer 3 times. Agarose beads were resuspended by 20 μl of hypotonic lysis buffer and 20 μl of 2× loading buffer and boiled at 100°C for 4 min.

Nascent peptide labeling by OP-puro—HEK293 cells (2.5 × 10^5 cells) were seeded in 24-well plate, cultured overnight, incubated with 20 μM OP-puro (Jena Bioscience) and RocA (0–3 μM) for 30 min, washed once with PBS, and then lysed with lysis buffer omitting DTT. The lysate was incubated with 1 μM IRDye800CW Azide (LI-COR Bioscience) for 30 min at 25°C, with Click-it cell reaction kit (Thermo Fisher scientific) according to manufacturer's instruction and run on SDS-PAGE. The gel images were acquired and quantified by ODYSSEY CLx (LI-COR Biosciences). Subsequently, total protein on the gel was stained by GelCode Blue Stain Reagent (Thermo Fisher scientific), then quantified by ODYSSEY CLx (LI-COR Biosciences), and used for the normalization of OP-puro labeled nascent protein signal.

Western blot—Anti-eIF4A1 (#2490S, Cell Signaling Technology), anti-eIF4A2 (ab31218, Abcam), anti-β-actin (926–42212, LI-COR Biosciences), and anti-SBP-tag (SB19-C4 sc-101595, Santa Cruz Biotechnology) were used as primary antibodies. IRDye 800CW anti-rabbit IgG (926–32211, LI-COR Biosciences) and IRDye 680RD anti-mouse IgG (925–68070, LI-COR Biosciences) were used as secondary antibodies. Images were captured by ODYSSEY CLx (LI-COR Biosciences).

In vitro* translation assay by the reconstituted system—In vitro* translation was performed basically as described elsewhere (Machida et al., 2018) (T. Yokoyama, K. Machida, W. Iwasaki, T. Shigeta, M. Nishimoto, M. Takahashi, A. Sakamoto, M. Yonemochi, Y. Harada, H. Shigematsu, M. Shirouzu, H. Tadakuma, H. Imataka, and T. Ito, personal communication). The purified components except for eIF4A1 were mixed with mRNA reporter containing the sequence coding for the *Renilla* luciferase and polypurine motifs in 5′ UTR. To 3 μl of this mixture, 1 μl of RocA aqueous dilutions were added. Since eIF4A1 is essential for translation, 1 μl of WT or Phe163Leu-Ile199Met mutant eIF4A1

protein solutions were added last to start the reaction, and the mixture was incubated at 32°C for 4 h. The final concentrations were 0.24 μM for each 40S and 60S ribosomal subunits, 50 nM for mRNA reporter with polypurine motifs in 5′ UTR, and 1.25 μM for WT or Phe163Leu-Ile199Met mutant eIF4A1 proteins. The translated *Renilla* luciferase was detected using the Dual-Glo Luciferase Assay System (Promega).

Synthesis of biotinylated RocA—All reactions were carried out under an argon atmosphere with dry solvents unless otherwise stated. Aglafoline (methyl rocaglate) was purchased from MedChem Express. Biotinylated rocaglate was prepared in 3 steps based on previously reported method as shown in Figure S1E (Chambers et al., 2016). To a stirred solution of methyl rocaglate (20.0 mg, 0.0406 mmol) in dry THF (5 ml) was added 0.2 M aqueous LiOH·H_2O solution (1.00 ml, 0.200 mmol) at room temperature. The resulting mixture was stirred at 60°C for 5 h. To the mixture was added 1 M HCl until pH ~2 at room temperature. The resulting mixture was extracted with Et_2O four times. The combined organic phases were washed with brine, dried over Na_2SO_4, filtered, and concentrated *in vacuo* to yield crude rocagloic acid, which was used for the next reaction without further purification. To a stirred solution of the above crude rocagloic acid in dry DCM (5.70 ml) were added DCC (52.0 mg, 0.252 mmol) and propargyl amine (25.6 μl, 0.400 mmol) at 0°C and the mixture was stirred at the same temperature for 5 min. Then, DMAP (23.5 mg, 0.192 mmol) was added to the mixture. After being stirred at room temperature for 34 h, to the reaction mixture were added CH_2Cl_2 and H_2O. One molar HCl was added until pH ~2 at 0°C and the mixture was stirred at room temperature for 30 min. The resulting mixture was extracted with DCM four times. The combined organic phases were washed with saturated aqueous $NaHCO_3$ solution, water, and brine, dried over Na_2SO_4, filtered, and concentrated *in vacuo*. The residue was purified by column chromatography (EtOAc:hexane = 1:1 to 2:1) to give propargyl amide (12.4 mg, 0.0241 mmol, 59% in 2 steps) as a white solid, which was used for the next reaction without further purification. To a 10 ml amber egg-plant shaped flask were added DMSO solution of TBTA (93.0 μl, 2.0 mg/ml, 0.351 μmol), aqueous solution of sodium ascorbate (35 μl, 20 mg/ml, 3.53 μmol), aqueous solution of $CuSO_4$ (28 μl, 2.0 mg/ml, 0.351 μmol), DMSO (200 μl), and H_2O (100 μl). After being stirred at room temperature for 10 min, to the mixture was added a solution of propargyl amide (6.0 mg, 0.0116 mmol) and azide biotin linker (9.6 mg, 0.0203 mmol) (Chambers et al., 2013) in DMSO (300 μl) and H_2O (150 μl). The resulting mixture was stirred at 40°C for 16 h. The solvent was removed by freeze drying and water was added to the residue. The resulting mixture was extracted with $CHCl_3$ four times. The combined organic phases were dried over Na_2SO_4, filtered, and concentrated *in vacuo*. The residue was purified by column chromatography (MeOH:EtOAc = 1:4 to 1:2) to give the biotinylated rocaglate (8.2 mg, 0.0083 mmol, 72%) as a white solid. This compound was spectroscopically identical to that previously reported (Chambers et al., 2016).

^{1}H NMR (400 MHz, $CDCl_3$): δ 8.08 (s, 1H), 7.48 (s, 1H), 7.12 (d, *J* = 8.7 Hz, 2H), 6.98–7.04 (m, 5H), 6.77 (s, 1H), 6.60 (d, *J* = 9.2 Hz, 2H), 6.47 (brs, 1H), 6.24 (d, *J* = 1.8 Hz, 1H), 6.07 (d, *J* = 2.1 Hz, 1H), 5.49 (brs, 1H), 4.86 (d, *J* = 4.6 Hz, 1H), 4.28–4.55 (m, 8H), 3.96 (dd, *J* = 14.0, 5.3 Hz, 1H), 3.816 (s, 3H), 3.808 (s, 3H), 3.65 (s, 3H), 3.50–3.62 (m, 11H), 3.34 (t, *J* = 5.7 Hz, 2H), 3.22–3.29 (m, 2H), 3.10–3.14 (m, 1H), 2.86 (dd, *J* = 12.6, 4.4 Hz,

1H), 2.69 (d, *J* = 12.9 Hz, 1H), 2.11 (t, *J* = 7.4 Hz, 2H), 2.03–2.06 (m, 2H), 1.56–1.74 (m, 6H), 1.37–1.46 (m, 2H). HRMS (ESI): Calculated for $C_{50}H_{65}N_7NaO_{12}S$ $[M+Na]^+$, 1010.4304: found, 1010.4309.

RocA-pulldown assay—In 20 μl reaction, recombinant eIF4A1 (WT or Phe163Leu-Ile199Met), 5′ FAM-labeled RNA $[(AG)_{10}$ or $(CAA)_6CA]$, and drug (RocA-bition or naïve RocA) were incubated at 10 μM each in 20 mM HEPES-NaOH pH 7.5, 150 mM NaCl, 1 mM DTT, 1% glycerol, 1 mM $MgCl_2$, and 1 mM AMPPNP for 15 min at 25°C. Ten μl of Dynabeads M-280 Streptavidin (Thermo Fisher scientific) equilibrated with buffer 1 (20 mM HEPES-NaOH pH 7.5, 150 mM NaCl, and 1 mM DTT) was resuspended by 5 μl of buffer 1, added to the reaction, and then incubated for 15 min at 25°C. After the beads were washed 5 times by buffer 1 containing 0.1% Triton-X 100, 1 mM $MgCl_2$, and 1 mM AMPPNP, protein and RNA were eluted by NuPAGE LDS Sample Buffer (Thermo Fisher scientific) and Trizol LS (Thermo Fisher scientific), respectively. The proteins run on the gel was visualized by GelCode Blue Stain Reagent (Thermo Fisher scientific), then the images were capture by LI-COR Odyssey CLx. FAM signals from RNAs on the gel was imaged by ImageQuant LAS-4000 (GE Healthcare).

QUANTIFICATION AND STATISTICAL ANALYSIS

Structure determination—An X-ray diffraction dataset was collected at ~100 K on the beamline BL41XU in SPring-8 (Hyogo, Japan), and processed with the program XDS (Kabsch, 2010). Further processes were performed using the program suite PHENIX (Adams et al., 2010). The initial phases were determined by the molecular replacement method using the program Phaser-MR (McCoy et al., 2007). The eIF4A1 NTD and CTD portions of the eIF4A•PDCD4 complex (PDB ID: 2ZU6) (Chang et al., 2009) were used as search models. The initial model was refined using the PHENIX AutoBuild wizard (Terwilliger et al., 2008), and the model was further manually refined using the software PHENIX phenix.refine (Adams et al., 2010) and Coot (Emsley and Cowtan, 2004). In the Ramachandran plot, 98.7% and 1.3% of the residues in the model are in the favored and allowed regions, respectively. The dataset and refinement statistics are summarized in Table 1. The molecular graphics were prepared with the program PyMol (Schrödinger).

***De novo* assembly of *Aglaia* transcriptome—**Transriptome was assembled with Trinity (Grabherr et al., 2011) and functionally annotated with Trinotate (Haas et al., 2013). *Azadirachita indica* transcriptome from the leaves (SRR518505) (Krishnan et al., 2012) was assembled similarly. The alignments of eIF4A homologs among eukaryote were depicted by ESPript 3.0 (http://espript.ibcp.fr) (Robert and Gouet, 2014). Sequences eIF4A homologs (94 in total) were obtained from Uniprot (referred to as "dead box helicase family eif4a subfamily") and NCBI homologene (referred to as "eukaryotic translation initiation factor 4A1" and "eukaryotic translation initiation factor 4A2"), without overlaps. Conservation matrix was calculated by AAcon (http://www.compbio.dundee.ac.uk/aacon/).

Phylogenetic tree—Phylogenetic tree of Meliaceae family plant was depicted using the sequences of RuBisCo large subunit by Clustal Omega (EMBL-EBI). The sequences were selected as previously reported (Krishnan et al., 2012). The accessions were as follows:

Aglaia elaeagnoidea: AY128209

Aglaia elliptica: AY128210

Aglaia formosana: FN599441

Aglaia odorata: this study,

ATGAGTTGTAGGGAGGGACTTATGTCACCACAAACAGAGACTAAAGCAAGT
GTTGGATTCAAAGCCGGTGTTAAAGATTATAAATTGACTTATTATACTCCTGAC
TATGTAACCAAAGATACTGATATCTTGGCAGCATTCCGAGTAACTCCTCAACC
CGGAGTTCCGCCCGAGGAAGCAGGAGCTGCGGTAGCTGCGGAATCCTCTAC
TGGTACATGGACAACTGTGTGGACCGATGGGCTTACTAGCCTTGATCGTTACA
AAGGACGATGCTACAACATTGAGCCCGTTGCTGGAGAAGAAAATCAATATAT
ATGTTATGTAGCTTACCCTTTAGACCTTTTTGAAGAAGGTTCTGTTACTAACAT
GTTTACGTCCATTGTGGGTAATGTATTTGGGTTCAAAGCCCTGCGCGCTCTAC
GTCTAGAGGATCTACGAATCCCGACCGCATATATTAAAACTTTCCAAGGTCCA
CCTCATGGGATCCAAGTTGAGAGAGATAAATTGAACAAGTATGGCCGTCCCC
TATTGGGATGTACTATTAAACCAAAATTGGGGTTATCCGCTAAGAATTACGGT
AGAGCAGTTTATGAATGTCTACGCGGTGGACTTGACTTTACCAAAGATGATG
AGAACGTGAACTCCCAACCATTTATGCGTTGGCGAGACCGTTTCGTATTTTGT
GCGGAAGCAATCTTTAAAGCACAAGCTGAAACAGGTGAAATCAAAGGTCAT
TACTTGAATGCTACTGCAGGTACATGCGAAGAAATGCTAAAAAGGGCTGTCT
TTGCCAGAGAGTTGGGAGCTCCTATCGTAATGCATGACTACTTAACAGGTGGA
TTCACCGCAAATACTAGCTTGGCTCATTATTGCCGAGATAATGGTCTACTTCTT
CACATCCACCGTGCAATGCATGCAGTTATTGATAGACAGAAAAATCATGGTAT
GCACTTTCGTGTACTAGCTAAAGCTCTACGTCTGTCTGGTGGAGATCATGTTC
ACTCTGGTACAGTAGTAGGTAAACTTGAAGGGGAAAGAGAAATAACTTTGG
GATTTGTTGATCAATTACGTGATGATTTTATTGAAAAAGATCGAAGCCGCGGG
AATTATTTCACTCAAGATTGGGTCTCTATACCAGGTGTTTTGCCCGTGGCTTCC
GGAGGTATTCACGTTTGGCATATGCCCGCTTTGACTGAAATCTTTGGAGATGA
TTCCGTACTACAATTCGGTGGAGGAACTTTAGGACACCCTTGGGGAAATGCA
CCCGGCGCCGTAGCTAATCGAGTAGCTCTAGAAGCATGTGTAAAAGCTCGTA
ATGAAGGACGCGATCTTGCTAGCGAAGGTAATGAAATTATCCGTGAGGCTAG
CAAATGGAGTCCTGAACTGGCTGCTGCTTGTGAAGTGTGGAAGGAGATCAA
ATTTGAATTCGAGGCAGTGGATATTTTGGATCCTTCGTAA

Aphanamixis polystachya: AY128213

Azadirachta indica: AJ402917

Cabralea canjerana: DQ238055

Calodecaryia crassifolia: AY128216

Capuronianthus mahafalensis: AJ402935

Carapa guianensis: AY128219

Carapa procera: JQ626164

Cedrela odorata: AJ402938

Chisocheton macrophyllus: AY128221

Chisocheton montanus: FJ976126

Chukrasia tabularis: AY128223

Cipadessa baccifera: U39083

Citrus sinensis: DQ864733

Dysoxylum arborescens: FN599448

Dysoxylum gaudichaudianum: AY128227

Dysoxylum pettigrewianum: FJ976130

Ekebergia capensis: AJ402947

Guarea costata: JQ625748

Guarea glabra: U39085

Guarea guidonia: JQ626153

Guarea silvatica: JQ626002

Heckeldora staudtii: AJ402959

Khaya anthotheca: AJ402964

Khaya nyasica: FN599452

Lansium domesticum: AY128232

Lepidotrichilia volkensii: DQ238061

Lovoa swynnertonii: AY128233

Malleastrum mandenense: DQ238062

Melia azedarach: AY128234

Melia dubia: U38859

Munronia pinnata: AY128237

Naregamia alata: DQ238059

Nymania capensis: U39084

Owenia vernicosa: DQ238063

Pseudobersama mossambicensis: DQ238064

Pseudocarapa nitidula: DQ238056

Pseudoclausena chrysogyne: DQ238065

Quivisianthe papinae: AY128239

Reinwardtiodendron kinabaluense: DQ238054

Ruagea pubescens: DQ238057

Schmardaea microphylla: U39081

Swietenia macrophylla: U39080

Swietenia mahagoni: FN599465

Synoum glandulosum: AY128242

Toona sinensis: FN599468

Trichilia cipo: JQ625928

Trichilia emetica: U39082

Trichilia euneura: JQ625863

Trichilia pallida: JQ626046

Trichilia schomburgkii: JQ625769

Turraea sericea: AY128245

Vavaea amicorum: DQ238066

Walsura tubulata: AJ403017

Xylocarpus granatum: AY289680

Xylocarpus moluccensis: DQ238071

Fragment molecular orbital calculations—*Ab initio* fragment molecular orbital (FMO) calculation (Fedorov and Kitaura, 2009; Fedorov et al., 2012; Tanaka et al., 2014) was performed on the crystal structure of the human eIF4A1•RocA•polypurine RNA complex.

In molecular modeling, AMPPNP, Mg ion, and crystal water molecules were deleted from the crystal structure of the human eIF4A1•AMPPNP•RocA•polypurine RNA complex. The assignment of the protonation state and the addition of hydrogen atoms were performed using the Protonate 3D function of Molecular Operating Environment (MOE) program package (Chemical Computing Group). Then energy minimization was done by optimizing only hydrogen atoms at the Amber10:EHT force field.

FMO quantum chemical calculation for the entire eIF4A1•RocA•polypurine RNA complex was performed using the ABINIT-MP software (http://www.ciss.iis.u-tokyo.ac.jp/software/). The second order Møller-Plesset perturbation (MP2) method (Mochizuki et al., 2004a; Mochizuki et al., 2004b) was used with the 6–31G* basis function as a theoretical calculation level; namely, FMO-MP2/6–31G* level of theory was used. As fragmentations of the molecules in the FMO calculations, amino acids from eIF4A1, base parts and backbone parts from RNA, and RocA, were considered as units. The application of such a fragmentation treatment allowed us to clarify the electronic structure of the whole complex and the detailed interaction energies between fragments such as RocA–RNA base, RocA–RNA backbone, RocA–amino acid, and amino acid–amino acid. The inter-fragment interaction energy (IFIE) were further decomposed into four energy components, i.e., electrostatic, exchange repulsion, charge transfer and higher order mixed term, and dispersion, by using the pair interaction energy decomposition analysis (PIEDA) (Fedorov and Kitaura, 2007; Tsukamoto et al., 2015).

DATA AND SOFTWARE AVAILABILITY

Accession numbers—Transcriptome data of *Aglaia odorata* (SRR5947159) and ribosome profiling data (GSE102720) used in this study were deposited in NCBI. The atomic coordinates and structure factors have been deposited in the Protein Data Bank (PDB) under the accession number 5ZC9. Original images used for the figures are deposited in the Mendeley database (https://data.mendeley.com/datasets/z9c8mn82k5/draft?a=693ee68e-f6e7-4007-a175-f874393e962e).

Supplementary Material

Refer to Web version on PubMed Central for supplementary material.

Acknowledgments

References

Adams PD, Afonine PV, Bunkóczi G, Chen VB, Davis IW, Echols N, Headd JJ, Hung LW, Kapral GJ, Grosse-Kunstleve RW, McCoy AJ, Moriarty NW, Oeffner R, Read RJ, Richardson DC, Richardson JS, Terwilliger TC, and Zwart PH (2010). PHENIX: a comprehensive Python-based system for macromolecular structure solution. Acta Crystallogr D Biol Crystallogr 66, 213–221. [PubMed: 20124702]

Andersen CB, Ballut L, Johansen JS, Chamieh H, Nielsen KH, Oliveira CL, Pedersen JS, Seraphin B, Le Hir H, and Andersen GR (2006). Structure of the exon junction core complex with a trapped DEAD-box ATPase bound to RNA. Science 313, 1968–1972. [PubMed: 16931718]

Bordeleau ME, Robert F, Gerard B, Lindqvist L, Chen SM, Wendel HG, Brem B, Greger H, Lowe SW, Porco JA, and Pelletier J (2008). Therapeutic suppression of translation initiation modulates chemosensitivity in a mouse lymphoma model. J Clin Invest 118, 2651–2660. [PubMed: 18551192]

Buchholz F, Ringrose L, Angrand PO, Rossi F, and Stewart AF (1996). Different thermostabilities of FLP and Cre recombinases: implications for applied site-specific recombination. Nucleic Acids Res 24, 4256–4262. [PubMed: 8932381]

Cencic R, Carrier M, Galicia-Vázquez G, Bordeleau ME, Sukarieh R, Bourdeau A, Brem B, Teodoro JG, Greger H, Tremblay ML, Porco JA, and Pelletier J (2009). Antitumor activity and mechanism of action of the cyclopenta[b]benzofuran, silvestrol. PLoS One 4, e5223. [PubMed: 19401772]

Chambers JM, Lindqvist LM, Savage GP, and Rizzacasa MA (2016). Total synthesis of a biotinylated rocaglate: Selective targeting of the translation factors eIF4AI/II. Bioorg Med Chem Lett 26, 262–264. [PubMed: 26718843]

Chambers JM, Lindqvist LM, Webb A, Huang DC, Savage GP, and Rizzacasa MA (2013). Synthesis of biotinylated episilvestrol: Highly selective targeting of the translation factors eIF4AI/II. Org Lett 15, 1406–1409. [PubMed: 23461621]

Chang JH, Cho YH, Sohn SY, Choi JM, Kim A, Kim YC, Jang SK, and Cho Y (2009). Crystal structure of the eIF4A-PDCD4 complex. Proc Natl Acad Sci U S A 106, 3148–3153. [PubMed: 19204291]

Chu J, Galicia-Vázquez G, Cencic R, Mills JR, Katigbak A, Porco JA, and Pelletier J (2016). CRISPR-mediated drug-target validation reveals selective pharmacological inhibition of the RNA helicase, eIF4A. Cell Rep 15, 2340–2347. [PubMed: 27239032]

Del Campo M, and Lambowitz AM (2009). Structure of the yeast DEAD box protein Mss116p reveals two wedges that crimp RNA. Mol Cell 35, 598–609. [PubMed: 19748356]

Delaglio F, Grzesiek S, Vuister GW, Zhu G, Pfeifer J, and Bax A (1995). NMRPipe: a multidimensional spectral processing system based on UNIX pipes. J Biomol NMR 6, 277–293. [PubMed: 8520220]

Emsley P, and Cowtan K (2004). Coot: model-building tools for molecular graphics. Acta Crystallogr D Biol Crystallogr 60, 2126–2132. [PubMed: 15572765]

Fedorov D, and Kitaura K (2009). The fragment molecular orbital method.

Fedorov DG, and Kitaura K (2007). Pair interaction energy decomposition analysis. J Comput Chem 28, 222–237. [PubMed: 17109433]

Fedorov DG, Nagata T, and Kitaura K (2012). Exploring chemistry with the fragment molecular orbital method. Phys Chem Chem Phys 14, 7562–7577. [PubMed: 22410762]

Floor SN, Borja MS, and Gross JD (2012). Interdomain dynamics and coactivation of the mRNA decapping enzyme Dcp2 are mediated by a gatekeeper tryptophan. Proc Natl Acad Sci U S A 109, 2872–2877. [PubMed: 22323607]

Floor SN, Condon KJ, Sharma D, Jankowsky E, and Doudna JA (2016). Autoinhibitory interdomain interactions and subfamily-specific extensions redefine the catalytic core of the human DEAD-box protein DDX3. J Biol Chem 291, 2412–2421. [PubMed: 26598523]

Grabherr MG, Haas BJ, Yassour M, Levin JZ, Thompson DA, Amit I, Adiconis X, Fan L, Raychowdhury R, Zeng Q, Chen Z, Mauceli E, Hacohen N, Gnirke A, Rhind N, di Palma F, Birren BW, Nusbaum C, Lindblad-Toh K, Friedman N, and Regev A (2011). Full-length transcriptome assembly from RNA-Seq data without a reference genome. Nat Biotechnol 29, 644–652. [PubMed: 21572440]

Haas BJ, Papanicolaou A, Yassour M, Grabherr M, Blood PD, Bowden J, Couger MB, Eccles D, Li B, Lieber M, Macmanes MD, Ott M, Orvis J, Pochet N, Strozzi F, Weeks N, Westerman R, William T, Dewey CN, Henschel R, Leduc RD, Friedman N, and Regev A (2013). *De novo* transcript sequence reconstruction from RNA-seq using the Trinity platform for reference generation and analysis. Nat Protoc 8, 1494–1512. [PubMed: 23845962]

Hinnebusch AG, Ivanov IP, and Sonenberg N (2016). Translational control by 5′-untranslated regions of eukaryotic mRNAs. Science 352, 1413–1416. [PubMed: 27313038]

Ingolia NT, Brar GA, Rouskin S, McGeachy AM, and Weissman JS (2012). The ribosome profiling strategy for monitoring translation in vivo by deep sequencing of ribosome-protected mRNA fragments. Nat Protoc 7, 1534–1550. [PubMed: 22836135]

Ingolia NT, Ghaemmaghami S, Newman JR, and Weissman JS (2009). Genome-wide analysis in vivo of translation with nucleotide resolution using ribosome profiling. Science 324, 218–223. [PubMed: 19213877]

Ishikawa K, Makanae K, Iwasaki S, Ingolia NT, and Moriya H (2017). Post-translational dosage compensation buffers genetic perturbations to stoichiometry of protein complexes. PLoS Genet 13, e1006554. [PubMed: 28121980]

Iwasaki S, Floor SN, and Ingolia NT (2016). Rocaglates convert DEAD-box protein eIF4A into a sequence-selective translational repressor. Nature 534, 558–561. [PubMed: 27309803]

Jankowsky E, and Putnam A (2010). Duplex unwinding with DEAD-box proteins. Methods Mol Biol 587, 245–264. [PubMed: 20225155]

Kabsch W (2010). XDS. Acta Crystallogr D Biol Crystallogr 66, 125–132. [PubMed: 20124692]

Krishnan NM, Pattnaik S, Jain P, Gaur P, Choudhary R, Vaidyanathan S, Deepak S, Hariharan AK, Krishna PB, Nair J, Varghese L, Valivarthi NK, Dhas K, Ramaswamy K, and Panda B (2012). A draft of the genome and four transcriptomes of a medicinal and pesticidal angiosperm *Azadirachta indica*. BMC Genomics 13, 464. [PubMed: 22958331]

Li-Weber M (2015). Molecular mechanisms and anti-cancer aspects of the medicinal phytochemicals rocaglamides (=flavaglines). Int J Cancer 137, 1791–1799. [PubMed: 24895251]

Lin S, Staahl BT, Alla RK, and Doudna JA (2014). Enhanced homology-directed human genome engineering by controlled timing of CRISPR/Cas9 delivery. Elife 3, e04766. [PubMed: 25497837]

Linder P, and Jankowsky E (2011). From unwinding to clamping - the DEAD box RNA helicase family. Nat Rev Mol Cell Biol 12, 505–516. [PubMed: 21779027]

Liu T, Nair SJ, Lescarbeau A, Belani J, Peluso S, Conley J, Tillotson B, O'Hearn P, Smith S, Slocum K, West K, Helble J, Douglas M, Bahadoor A, Ali J, McGovern K, Fritz C, Palombella VJ, Wylie A, Castro AC, and Tremblay MR (2012). Synthetic silvestrol analogues as potent and selective protein synthesis inhibitors. J Med Chem 55, 8859–8878. [PubMed: 23025805]

Machida K, Shigeta T, Yamamoto Y, Ito T, Svitkin Y, Sonenberg N, and Imataka H (2018). Dynamic interaction of poly(A)-binding protein with the ribosome. Sci Rep 8, 17435. [PubMed: 30487538]

Malina A, Mills JR, and Pelletier J (2012). Emerging therapeutics targeting mRNA translation. Cold Spring Harb Perspect Biol 4, a012377. [PubMed: 22474009]

Manier S, Huynh D, Shen YJ, Zhou J, Yusufzai T, Salem KZ, Ebright RY, Shi J, Park J, Glavey SV, Devine WG, Liu CJ, Leleu X, Quesnel B, Roche-Lestienne C, Snyder JK, Brown LE, Gray N, Bradner J, Whitesell L, Porco JA, and Ghobrial IM (2017). Inhibiting the oncogenic translation program is an effective therapeutic strategy in multiple myeloma. Sci Transl Med 9,

McCoy AJ, Grosse-Kunstleve RW, Adams PD, Winn MD, Storoni LC, and Read RJ (2007). Phaser crystallographic software. J Appl Crystallogr 40, 658–674. [PubMed: 19461840]

McGlincy NJ, and Ingolia NT (2017). Transcriptome-wide measurement of translation by ribosome profiling. Methods 126, 112–129. [PubMed: 28579404]

Mochizuki Y, Koikegami S, Nakano T, Amari S, and Kitaura K (2004a). Large scale MP2 calculations with fragment molecular orbital scheme. Chemical Physics Letters 396, 473–479.

Mochizuki Y, Nakano T, Koikegami S, Tanimori S, Abe Y, Nagashima U, and Kitaura K (2004b). A parallelized integral-direct second-order Møller–Plesset perturbation theory method with a fragment molecular orbital scheme. Theoretical Chemistry Accounts 112, 442–452.

Mori S, Abeygunawardana C, Johnson MO, and van Zijl PC (1995). Improved sensitivity of HSQC spectra of exchanging protons at short interscan delays using a new fast HSQC (FHSQC) detection scheme that avoids water saturation. J Magn Reson B 108, 94–98. [PubMed: 7627436]

Morisaki T, Lyon K, DeLuca KF, DeLuca JG, English BP, Zhang Z, Lavis LD, Grimm JB, Viswanathan S, Looger LL, Lionnet T, and Stasevich TJ (2016). Real-time quantification of single RNA translation dynamics in living cells. Science 352, 1425–1429. [PubMed: 27313040]

Mueller L (1979). Sensitivity enhanced detection of weak nuclei using heteronuclear multiple quantum coherence. J Am Chem Soc 101, 4481–4484.

Mullard A (2017). Small molecules against RNA targets attract big backers. Nat Rev Drug Discov 16, 813–815. [PubMed: 29180732]

O'Gorman S, Fox DT, and Wahl GM (1991). Recombinase-mediated gene activation and site-specific integration in mammalian cells. Science 251, 1351–1355. [PubMed: 1900642]

Pommier Y, Kiselev E, and Marchand C (2015). Interfacial inhibitors. Bioorg Med Chem Lett 25, 3961–3965. [PubMed: 26235949]

Robert X, and Gouet P (2014). Deciphering key features in protein structures with the new ENDscript server. Nucleic Acids Res 42, W320–4. [PubMed: 24753421]

Rogers GWJ, Komar AA, and Merrick WC (2002). eIF4A: the godfather of the DEAD box helicases. Prog Nucleic Acid Res Mol Biol 72, 307–331. [PubMed: 12206455]

Rubio CA, Weisburd B, Holderfield M, Arias C, Fang E, DeRisi JL, and Fanidi A (2014). Transcriptome-wide characterization of the eIF4A signature highlights plasticity in translation regulation. Genome Biol 15, 476. [PubMed: 25273840]

Ruggero D (2013). Translational control in cancer etiology. Cold Spring Harb Perspect Biol 5,

Sadlish H, Galicia-Vazquez G, Paris CG, Aust T, Bhullar B, Chang L, Helliwell SB, Hoepfner D, Knapp B, Riedl R, Roggo S, Schuierer S, Studer C, Porco JA, Pelletier J, and Movva NR (2013). Evidence for a functionally relevant rocaglamide binding site on the eIF4A-RNA complex. ACS Chem Biol 8, 1519–1527. [PubMed: 23614532]

Santagata S, Mendillo ML, Tang YC, Subramanian A, Perley CC, Roche SP, Wong B, Narayan R, Kwon H, Koeva M, Amon A, Golub TR, Porco JAJ, Whitesell L, and Lindquist S (2013). Tight coordination of protein translation and HSF1 activation supports the anabolic malignant state. Science 341, 1238303. [PubMed: 23869022]

Sen ND, Zhou F, Ingolia NT, and Hinnebusch AG (2015). Genome-wide analysis of translational efficiency reveals distinct but overlapping functions of yeast DEAD-box RNA helicases Ded1 and eIF4A. Genome Res 25, 1196–1205. [PubMed: 26122911]

Sengoku T, Nureki O, Nakamura A, Kobayashi S, and Yokoyama S (2006). Structural basis for RNA unwinding by the DEAD-box protein *Drosophila* Vasa. Cell 125, 287–300. [PubMed: 16630817]

Sonenberg N, and Hinnebusch AG (2009). Regulation of translation initiation in eukaryotes: mechanisms and biological targets. Cell 136, 731–745. [PubMed: 19239892]

Svitkin YV, Pause A, Haghighat A, Pyronnet S, Witherell G, Belsham GJ, and Sonenberg N (2001). The requirement for eukaryotic initiation factor 4A (elF4A) in translation is in direct proportion to the degree of mRNA 5′ secondary structure. RNA 7, 382–394. [PubMed: 11333019]

Tanaka S, Mochizuki Y, Komeiji Y, Okiyama Y, and Fukuzawa K (2014). Electron-correlated fragment-molecular-orbital calculations for biomolecular and nano systems. Phys Chem Chem Phys 16, 10310–10344. [PubMed: 24740821]

Terwilliger TC, Grosse-Kunstleve RW, Afonine PV, Moriarty NW, Zwart PH, Hung LW, Read RJ, and Adams PD (2008). Iterative model building, structure refinement and density modification with the PHENIX AutoBuild wizard. Acta Crystallogr D Biol Crystallogr 64, 61–69. [PubMed: 18094468]

Tsukamoto T, Kato K, Kato A, Nakano T, Mochizuki Y, and Fukuzawa K (2015). Implementation of pair interaction energy decomposition analysis and its applications to protein-ligand systems. Journal of Computer Chemistry, Japan 14, 1–9.

Wang C, Han B, Zhou R, and Zhuang X (2016). Real-time imaging of translation on single mRNA transcripts in live cells. Cell 165, 990–1001. [PubMed: 27153499]

Wolfe AL, Singh K, Zhong Y, Drewe P, Rajasekhar VK, Sanghvi VR, Mavrakis KJ, Jiang M, Roderick JE, Van der Meulen J, Schatz JH, Rodrigo CM, Zhao C, Rondou P, de Stanchina E, Teruya-Feldstein J, Kelliher MA, Speleman F, Porco JA, Pelletier J, Rätsch G, and Wendel HG (2014). RNA G-quadruplexes cause eIF4A-dependent oncogene translation in cancer. Nature 513, 65–70. [PubMed: 25079319]

Wu B, Eliscovich C, Yoon YJ, and Singer RH (2016). Translation dynamics of single mRNAs in live cells and neurons. Science 352, 1430–1435. [PubMed: 27313041]

Yan X, Hoek TA, Vale RD, and Tanenbaum ME (2016). Dynamics of translation of single mRNA molecules *in vivo*. Cell 165, 976–989. [PubMed: 27153498]
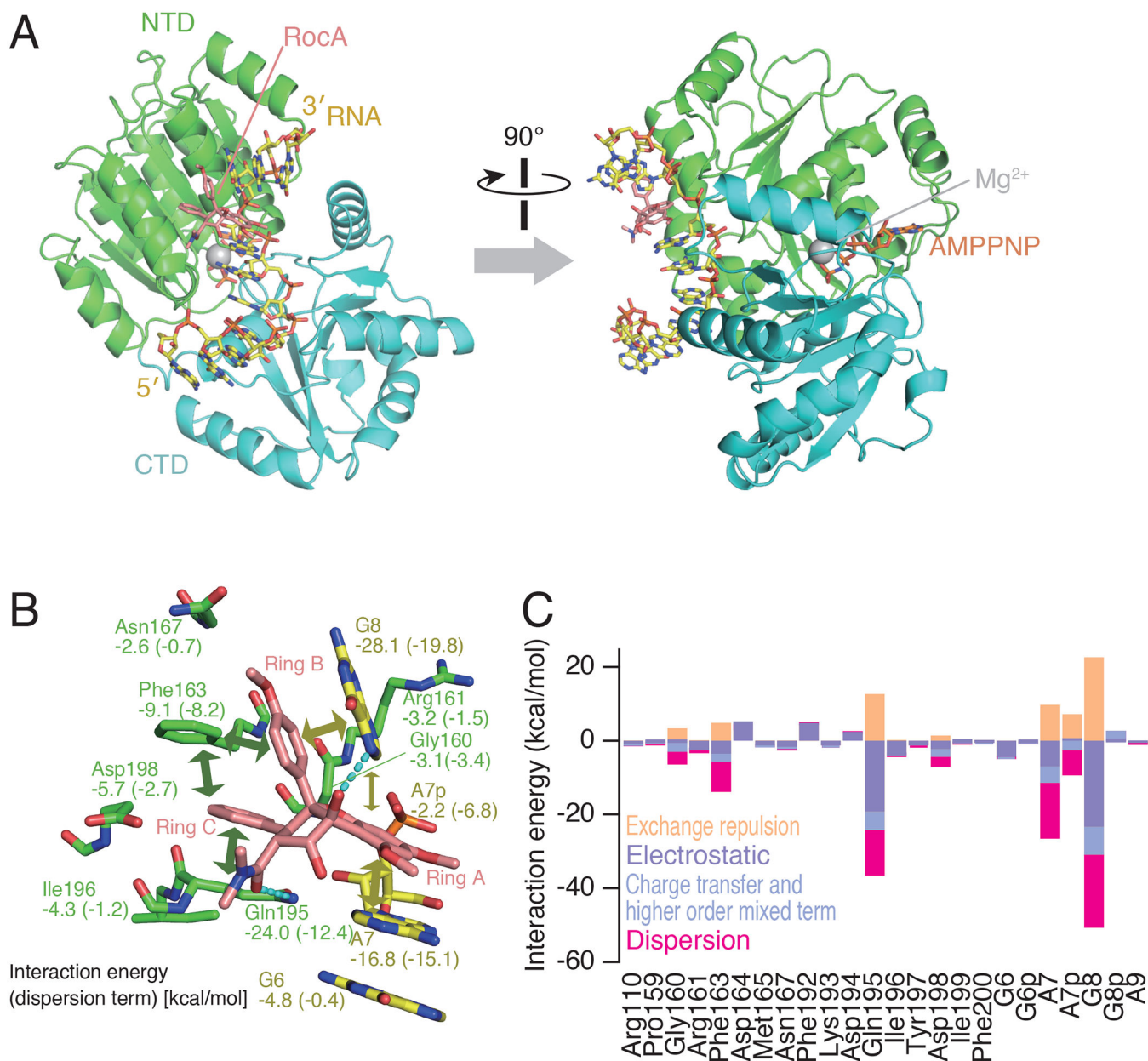
Figure 1. Quaternary structure of the human eIF4A1•AMPPNP•RocA•polypurine RNA complex.

A. The overall crystal structure of the human eIF4A1•AMPPNP•RocA•polypurine RNA complex shown by surface and sphere representations. Human eIF4A1 NTD; green surface, CTD; cyan surface, RNA; yellow surface, magnesium ion; gray ball, and RocA; salmon spheres.

B and C. Estimated interaction energy terms (C) between RocA and RNA/protein by FMO calculation and their representations along the RocA-binding pocket in the structure (B). RocA-protein interactions; dark green double-headed arrows, RocA-RNA interactions; dark yellow double-headed arrows, and hydrogen bonds with RocA; dashed light blue lines.

Interaction energies between each fragment pair are depicted in B. Dispersion terms are in parenthesis.
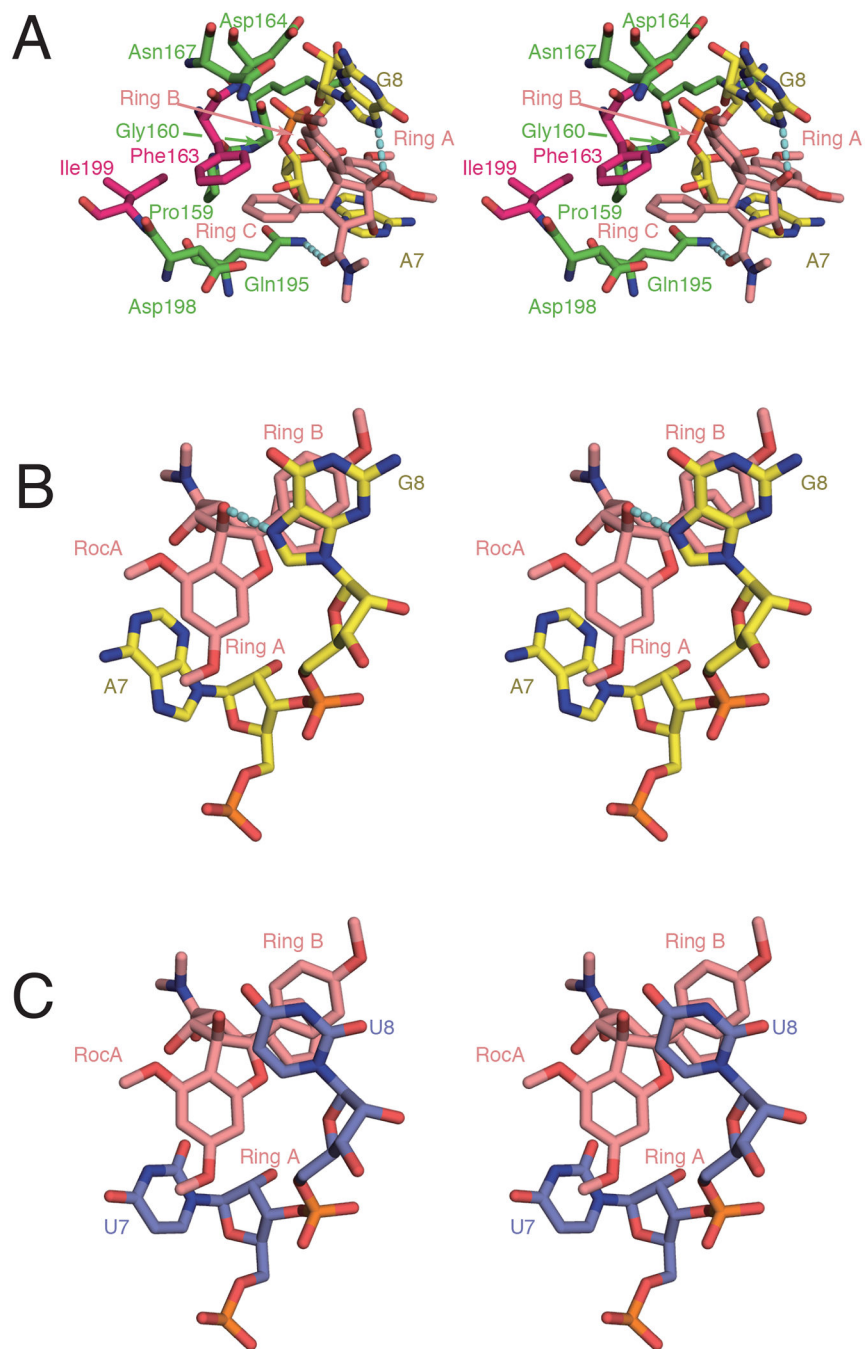See also Figure S1.

Figure 2. Purine selectivity accomplished by RocA.

A. RocA and its interacting residues in eIF4A1 and polypurine RNA (wall-eyed stereo view). The residues from the eIF4A1 NTD and RNA, and RocA are shown by stick models and colored as in Figure 1. *Aglaia*-specific amino acid substitutions (Figure 3) are colored magenta.

B and C. Structural comparison of RocA and the interacting RNAs (wall-eyed stereo view). RocA, A7 and G8 determined in this study (B), and RocA, U7 and U8 modeled based on the

structure determined in this study (C), are shown by stick models, and colored as in Figure 1, except that the modeled U7 and U8 are colored purple.

Dashed light blue lines indicate hydrogen bonds.
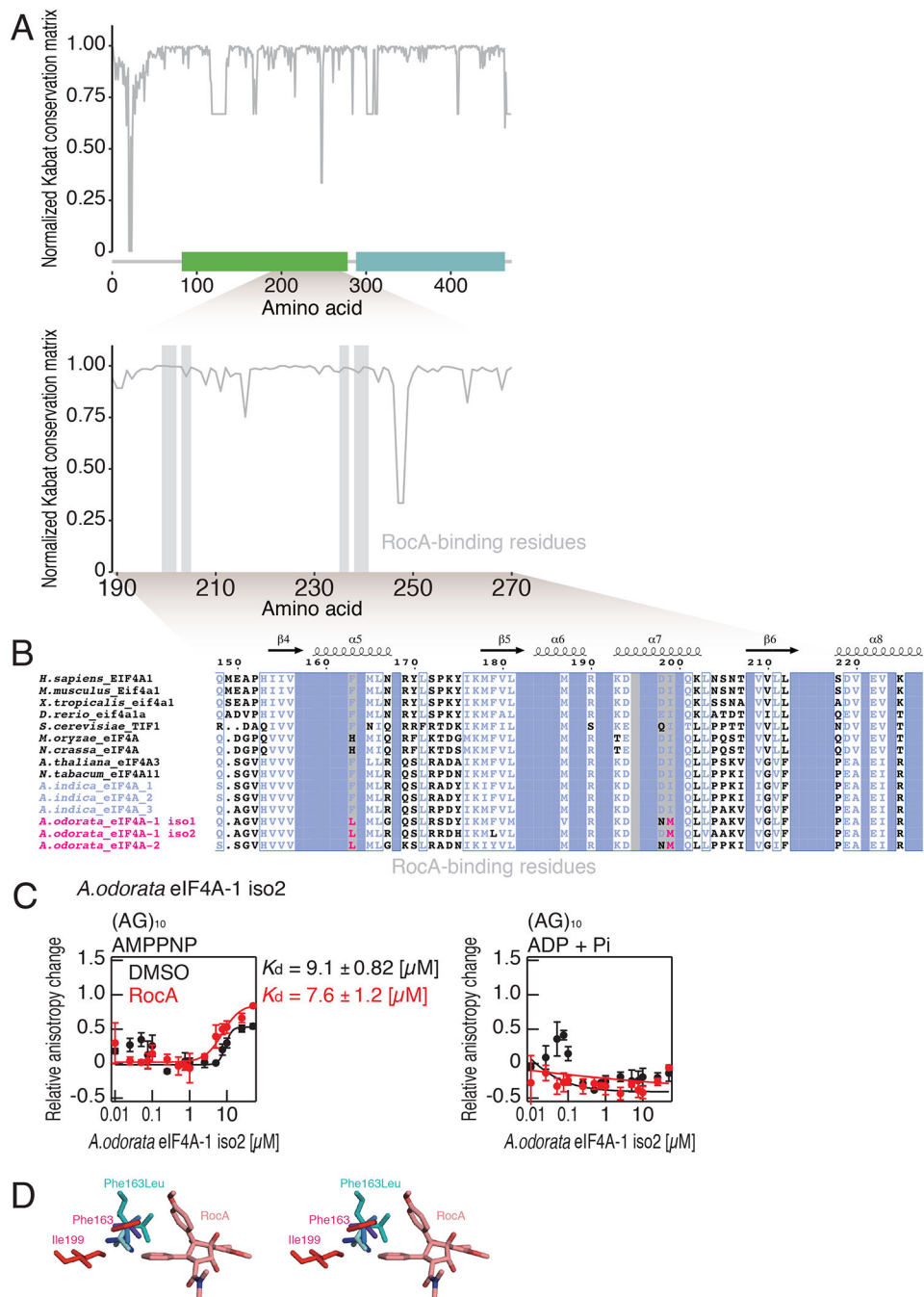
See also Figure S2.

Figure 3. Distinctive amino acid substitutions in *Aglaia* eIF4A revealed by *de novo* transcriptome assembly.

A. Normalized Kabat conservation matrix calculated from 94 eIF4A homologs registered in Uniprot and NCBI homologene.

B. Alignment of eIF4A sequences among representative eukaryotes and Meliaceae family plants, including *Aglaia odorata* and *Azadirachita indica*. Amino acid position in human eIF4A1 is shown.

C. Conventional RNA binding assays between recombinant *Aglaia* eIF4A protein and polypurine RNA. Affinities were measured by fluorescence polarization with 5′ FAM-labeled $(AG)_{10}$ RNAs.

D. RocA and five possible rotamers of modeled Leu residues (blue colors) at Phe163 residues (wall-eyed stereo view). In C, data represent mean and S.D. (n = 3).
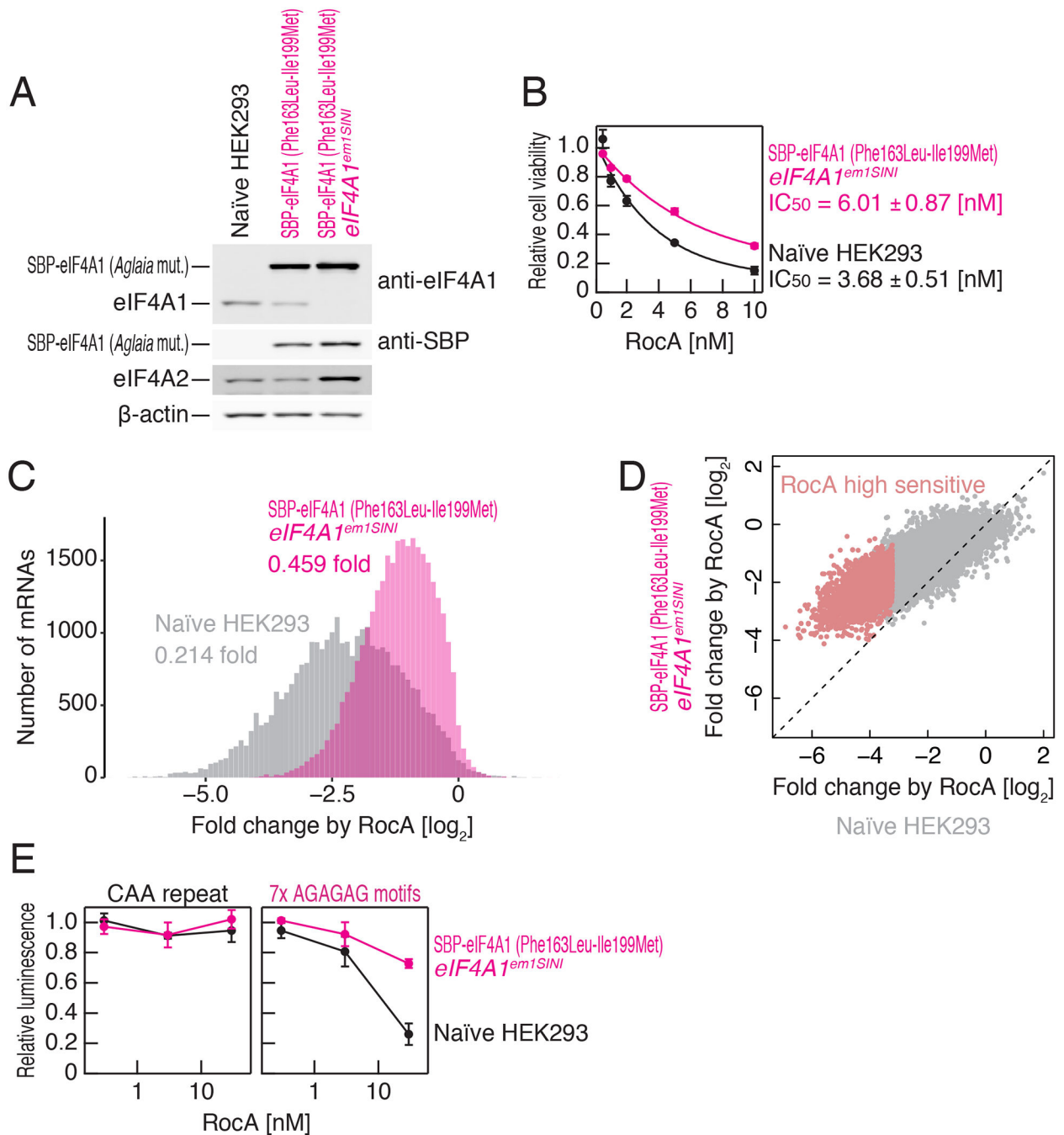
See also Figure S3 and Table S1.

Figure 4. Phe163Leu-Ile199Met mutations in eIF4A1 confer RocA-resistance on HEK293 cells.
A. Western blot analyses of eIF4A1 from SBP-eIF4A1 (Phe163Leu-Ile199Met) $eIF4A1^{SINI}$ HEK293 cells, which are established by the combination of Flp-In system integration and CRISPR/Cas9 genome editing (Figure S5).

B. Cell viability of SBP-eIF4A1 (Phe163Leu-Ile199Met) $eIF4A1^{SINI}$ HEK293 cells upon RocA treatment.

C. Histogram representing the distribution of mRNAs along translation change by RocA. Naïve HEK293 cells and SBP-eIF4A1 (Phe163Leu-Ile199Met) $eIF4A1^{SINI}$ HEK293 cells

were treated with 0.3 μM RocA and used for ribosome profiling. Mitochondrial ribosome footprints were used as the internal spike-in control as described previously (Iwasaki et al., 2016). Bin width is 0.1.

D. Scatter plot representing mRNA translation change by RocA treatment. Dots indicate translation changes of the mRNAs in naïve and SBP-eIF4A1 (Phe163Leu-Ile199Met) *eIF4A1^SINI* HEK293 cells. RocA-high sensitivity mRNAs defined in naïve HEK cells are highlighted.

E. Reporter assays with mRNAs possessing CAA-repeat or polypurine motifs in 5′ UTR. In B and E, data represent mean and S.D. (n = 3).
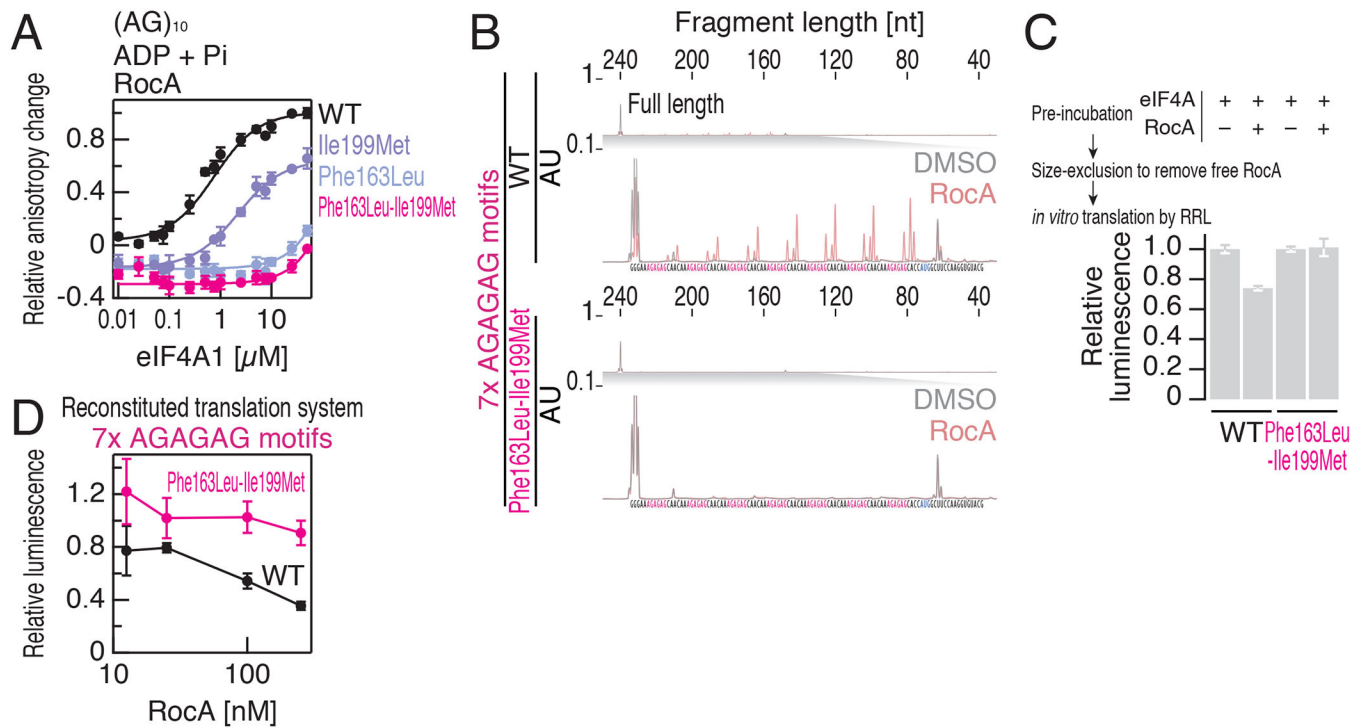
See also Figure S4 and S5.

Figure 5. Double mutant eIF4A1 is defective in ATP-independent polypurine RNA binding upon RocA treatment.

A. Conventional RNA binding assays between recombinant wild-type (WT) and mutated eIF4A1 proteins and polypurine RNA, in the presence of ADP, Pi, and RocA. Affinities were measured by fluorescence polarization with $5'$ FAM-labeled $(AG)_{10}$ RNAs.

B and C. The formation of eIF4A1•RocA complex on polypurine motifs on reporter mRNAs monitored by toeprinting assays (B), and following *in vitro* translation assays in rabbit rabbit reticulocyte lysates (C).

D. *In vitro* translation assays by the reconstituted pure system with human factors under a series of RocA concentrations. WT or double mutant eIF4A1 proteins were supplemented into the reactions. mRNA reporter with polypurine motifs in $5'$ UTR was used.

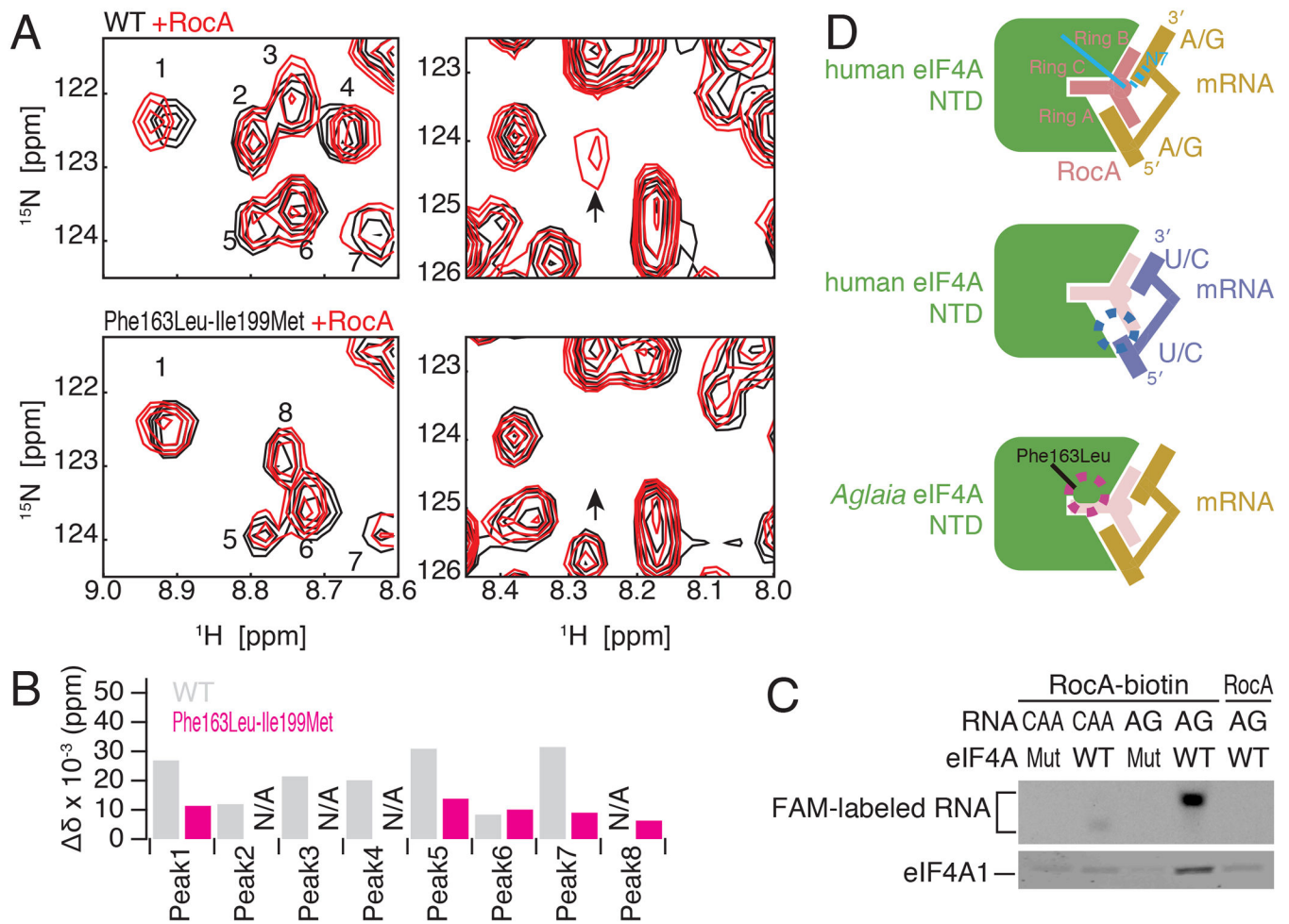In A, C, and D, data represent mean and S.D. (n = 3).

Figure 6. RocA targets a cavity formed between eIF4A1 and purines.

(A and B) NMR assays of ^{15}N-labeled eIF4A NTD of WT and double-mutant proteins in the absence or presence of RocA (A), and quantification of peaks (B). Arrows indicate the regions of chemical shifts observed upon RocA treatment.

C. Pulldown assays via biotinylated RocA with recombinant eIF4A1 (WT or double mutant) and 5′ FAM-labeled RNA [(AG)$_{10}$ or (CAA)$_6$CA].

D. Schematic representations of biomolecular-cavity targeting by RocA. Red and blue dotted circles represent steric hindrance and the weakened contact, respectively

See also Figure S6.

Table 1.

Data collection and refinement statistics

	Human eIF4A • AMPPNP • RocA • (AG)$_5$ complex
Data collection	
Space group	I2 2 2
Unit cell	
a, b, c (Å)	68.51, 100.26, 155.42
α, β, γ (°)	90, 90, 90
Wavelength (Å)	1.00000
Resolution range (Å)	45.73 – 2.00 (2.12 – 2.00)
Total reflections	242759 (37414)
Unique reflections	36572 (5794)
Multiplicity	6.6 (6.4)
Completeness (%)	99.8 (99.3)
$I/\sigma I$	11.51 (1.80)
R_{sym}	0.134 (1.022)
CQ$_{1/2}$	0.997 (0.793)
Refinement	
Resolution (Å)	45.73 – 2.00
Reflection used in refinement	36502
R_{work} / R_{free}	0.1929/0.2305
Number of non-hydrogen atoms	
Protein or RNA	3243
Ligand or ion	69
Water	246
R.m.s. deviations	
Bond length (Å)	0.004
Bond angles (°)	0.69
B-factors	
Protein or RNA	36.13
Ligand or ion	29.41
Water	39.84

Statistics for the highest-resolution shell are shown in parentheses.